Applied Thermal Engineering 194 (2021) 117087

Contents lists available at ScienceDirect

Applied Thermal Engineering

journal homepage: www.elsevier.com/locate/apthermeng

A review of heat pipe technology for foldable electronic devices

Michael J. Gibbons [a,*], Marco Marengo [b], Tim Persoons [a]

[a] Department of Mechanical, Manufacturing & Biomedical Engineering, Trinity College Dublin, The University of Dublin, Dublin 2, Ireland
[b] Advanced Engineering Centre, University of Brighton, BN2 4GJ Brighton, UK

ARTICLE INFO

Keywords:
Electronic cooling
Flexible heat pipe
Thermal ground plane
Thermal spreader
Vapor chamber
Thermal management

ABSTRACT

The advent of foldable and wearable devices, such as the Samsung Galaxy Fold (2019) and Huawei Mate X (2019), require increased battery size and processor performance to drive their larger flexible displays. There is a growing need to develop flexible thermal management solutions to cool these foldable electronic devices. This research presents a comprehensive review of the state-of-the-art for both rigid and flexible ultra-thin heat pipe technology. This review discusses various types of heat pipes, their thermal performance, novel manufacturing processes, and the open research questions, challenges, together with the potential future directions of this research area.

1. Introduction

Thermal management of mobile electronic devices is governed by user comfort, limiting operating performance [1,2]. Mobile electronic devices such as smartphones and tablets are trending towards lower thickness and increased functionality, leading to higher heat generation density from active components. The emergence of foldable and wearable devices, such as the Samsung Galaxy Fold and Huawei Mate X, require increased battery sizes and CPU performance to drive larger flexible displays. This results in increased generated heat fluxes [3], which is a primary reason for malfunctions and safety concerns [4].

Active air cooling or large heat sinks are not suitable to remove the generated thermal energy due to consumer-driven size requirements. Thus, the skin temperature and, consequently, mobile device performance are limited by natural convection cooling from the device's outer shell [5]. Natural convection cooling is a passive cooling strategy that is primarily dependent on the mobile device surface area and the temperature difference between the outer casing and surrounding ambient conditions [6], the latter of which is predominantly fixed by user comfort.

Device hotspots can also impact battery performance [7], and temperature differences as low as 1–2 °C can negatively diminish luminescence intensity across an OLED display [8–10], impacting the user experience. Thus, to optimize device performance and skin temperature, the generated thermal energy from the CPU, battery, and other active components must be spread across the entire device surface, enhancing natural convection cooling [8]. Ultra-thin vapour chambers may offer a viable solution to passively spread the generated thermal energy within mobile devices and increase thermal capacity for transient conditions. A vapour chamber or a flat plate heat pipe is a highly efficient, two-phase cooling solution that passively transports heat from a localized source to a much larger heat rejection surface. Tang et al. [1] defined an ultra-thin heat pipe as having a thickness <2 mm, and we will follow that precedent in this review. All heat pipes with a thickness >2 mm will be considered "macro". Rigid heat pipes will refer to heat pipes that are not designed to be flexed or folded, and flexible heat pipes are designed to fold. These categories are listed in Table 1.

Rigid heat pipes are a well-established and widely applied technology for use with mobile devices. However, in the case of foldable electronics, if the heat-generating components are concentrated in one section of the device, more than 50% of the cooling area is removed as heat cannot be effectively transported through an articulating joint. As a result, there is a growing demand to develop heat pipes with flexible adiabatic sections and ultra-thin, flexible vapour chambers [3].

Heat pipe technology also finds natural application in emerging thin and light portable computers, where thermal dissipation constraints limit the use of higher power processors and clock speeds to achieve increased performance. In June 2020, Intel announced the launch of their new 3D stacked 7 W Lakefield CPUs. These CPUs will find homes in premium, always connected thin and light laptops, such as the ThinkPad X1 fold (2020), Microsoft Surface Neo (2021), and Samsung Galaxy Book S (2020). Effective thermal transport and dissipation of thermal powers >20 W for packages sizes <2 mm is essential in enabling these next-generation thin and light computers to achieve optimal performance [1]. Ultra-thin rigid and flexible heat pipes have a largely shared

* Corresponding author.
E-mail address: Michael.Gibbons@tcd.ie (M.J. Gibbons).

https://doi.org/10.1016/j.applthermaleng.2021.117087
Received 25 January 2021; Received in revised form 27 April 2021; Accepted 9 May 2021
Available online 13 May 2021

Nomenclature

A	area [m^2]
C_l	wetted perimeter [m]
d	diameter [m]
f	friction factor
g	gravitational acceleration [$m\ s^{-2}$]
H	thickness [m]
h_{fg}	latent heat of vapourization [$kJ\ kg^{-1}$]
K	permeability [m^2]
k	thermal conductivity [$W\ m^{-1}\ K^{-1}$]
L	length [m]
M	figure of merit
N	mesh number/count [pores per inch]
P	pressure [$N\ m^{-2}$]
q	heat transfer rate [W]
q''	heat flux [$W\ m^{-2}$]
R	thermal resistance [$K\ W^{-1}$]
R_g	gas constant [$J\ kg^{-1}\ K^{-1}$]
r	radius [m]
T	temperature [K]
W	width [m]
w	spacing between wires [m]

Subscript

ave	average
bend	bending
c	curvature
cap	capillary
char	characteristic
cond	condenser
eff	effective
evap	evaporator
g	gravity
h	hydraulic
incl	inclination relative to horizontal
f	flow
l	liquid
max	maximum
p	pore
v	vapour
w	wire
∞	ambient

Greek symbol

Δ	differential [–]
ε	porosity [%]
θ	contact angle [°]
μ	dynamic viscosity [$Ns\ m^{-2}$]
ρ	density [$kg\ m^{-3}$]
σ	surface tension [$N\ m^{-1}$]
υ	vapour velocity [$m\ s^{-1}$]
ϕ	angle [°]

Acronyms

CTS	coefficient of thermal spreading
CPU	central processing unit
GPU	graphical processing unit
MOGA	multi-objective genetic algorithm
TDP	thermal design power

Table 1
Heat pipe category definition in the present review.

Category	Thickness	Designed for flexibility
Macro rigid heat pipe	>2 mm	No
Ultra-thin heat pipe	<2 mm	No
Macro flexible heat pipe	>2 mm	Yes
Ultra-thin flexible heat pipe	<2 mm	Yes

core design. The ultra-thin flexible heat pipe can be considered a bifurcation from rigid heat pipe technology, adding design complexity from their foldable requirement. As such, any discussion on ultra-thin flexible heat pipes should include their rigid counterparts to build a complete understanding of the current state-of-the-art and potential future development direction.

Table 2 assembles the prominent foldable and flexible consumer mobile electronic devices. All devices, except the Lenovo X1 fold, utilizes the same processors class as their non-flexible counterparts. These processors have a thermal design power (TDP) of 5–6 W and use natural convection cooling from the phone chassis to dissipate the generated fluxes. A mix and combination of heat pipes, thermal pads, and spreader plates are implemented to manage these devices thermally. The Lenovo X1 fold uses an Intel Core i5-L16G7 processor with a 7 W TDP. The increased thermal power is dissipated by forced convection using a combination of a heat pipe, thermal spreader, and fan cooling.

The increased unfolded surface area of these flexible devices should result in a greater cooling potential than their non-flexible counterparts. However, as noted from their thermal management systems, only the Huawei Mate Xs implements a solution to transfer heat from the high heat-generating components on the motherboard across the articulating joint. This means ~50% of the listed phones' surface area is not utilized in cooling the devices.

The emergence of foldable and wearable devices has resulted in a growing number of patent applications surrounding these technologies. These patents can be categorised into flexible devices [9,10,19–28,11,29,30,12–18], screens [31–39], circuits [40,41], wearables [42–44], and heat transfer approaches [45–53] from prominent companies such as Apple [9,10,35,39], Nokia [18,19,54], Samsung [20,21,52], LG [13,30,37,38], Intel [11], Huawei [53], Motorola [17], Sony [14], Lenovo [12], Microsoft [16], and Dell [55], among others.

Samsung [52] detailed a "*heat diffusion member*" placed at the foldable joint of a flexible electronic device. The described device design is similar in structure to their Samsung Galaxy Z Fold 2 (2020). One of the discussed potential implementations of the heat diffusion member at the device joint could be a flexible heat pipe, but its construction and design are not detailed. AURAS Technology [45] disclosed a flexible vapour chamber design for electronic devices. Their design outlines flexible top and bottom layers with a capillary structure disposed on the lower layer. Huawei [53] patented a thermal pad consisting of a compressible porous mesh structure and an organic compound that fills the porous structure. Kelvin Thermal Technologies [46,56] detailed a flexible thermal ground plane. The described design consists of micro-wicking micromesh coupled with nanorods, while the flexible shell material may be constructed from "*numerous layers, liquid crystal polymers, Kapton, or other polymers materials*."

Microsoft [49] disclosed a thermal management control system for foldable electronic devices. The control system compares the local temperature at two locations in separate foldable sections of the device, adjusting the processor performance based on the temperature differential. Microsoft [50,51] patented a heat transfer device comprising a vapour chamber and a flexible hinge. In their outlined design, "*an electronic device comprising a first portion and a second portion connected by*

Table 2
Prominent foldable and flexible mobile electronic devices.

Prominent Foldable Devices	Release date	Processor	Battery	Dimension (unfolded)	Thermal solution
Royole Flexpai	Dec 2018	Qualcomm Snapdragon 855, TDP: 5 W	3,970 mAh	190.3 × 134.0 × 7.6 mm^3	Natural convection. Thermal paste contact to metal chassis. No heat transfer across the flexible joint.
Samsung Galaxy Fold	Sept 2019	Qualcomm Snapdragon 855, TDP: 5 W	4,380 mAh	160.90 × 117.9 × 6.9 mm^3	Natural convection. Thermal spreader plate and thermal interface pad, no transfer across the flexible joint. Copper layer below both sections of the primary screen, not connected.
LG G8X ThinQ (Dual screen mode)	Nov 2019	Qualcomm Snapdragon 855, TDP: 5 W	4,000 mAh	165.96 × 84.63 × 14.99 mm^3 (with case)	Natural convection. Heat pipe. No heat transfer across the flexible joint.
Huawei Mate X	Nov 2019	Kirin 980, TDP: 6 W	4,500 mAh	161.3 × 146.2 × 5.4 mm^3	Natural convection. Thermal paste and heat pipe adjacent to the motherboard. No heat transfer across the flexible joint.
Samsung Galaxy Z Flip	Feb 2020	Qualcomm Snapdragon 855 Plus, TDP: 5 W	3,300 mAh	167.3 × 73.6 × 7.2 mm^3	Graphite thermal pad adjacent to the motherboard. No heat transfer across the flexible joint.
Moto Razr	Feb 2020	Qualcomm Snapdragon 710, TDP: 6 W	2,510 mAh	172.0 × 72.0 × 6.9 mm^3	Natural convection. Copper layer below primary battery and motherboard section. No heat transfer across the flexible joint.
Huawei Mate Xs	Mar 2020	Kirin 990, TDP: 6 W	4,500 mAh	161.3 × 146.2 × 5.4 mm^3	Natural convection. Thermal paste and heat Pipe adjacent to the motherboard, Graphite pad to transfer heat across the flexible joint.
Samsung Galaxy Z Fold 2	Sept 2020	Qualcomm Snapdragon 865 Plus, TDP: 5 W	4,500 mAh	159.2 × 128.2 × 6.9 mm^3	Natural convection. Graphite thermal pad adjacent to the motherboard. Copper layer below three screens. No heat transfer across the flexible joint.
Microsoft Surface Duo	Sept 2020	Qualcomm Snapdragon 855, TDP: 5 W	3,577 mAh	186.9 × 145.2 × 4.8 mm^3	Natural convection. Copper layer below screens. Copper foil and graphite tape on the motherboard side. No heat transfer across the flexible joint.
Lenovo ThinkPad X1 Fold	Sept 2020	Intel Core i5-L16G7, TDP: 7 W	50 Wh	299.4 × 236 × 11.5 mm^3	Forced convection. Vapour chamber, a thermal spreader to cool CPU top and bottom with a cooling fan for dissipation. No heat transfer across the flexible joint.
Royole Flewxpai 2	Sept 2020	Qualcomm Snapdragon 865, TDP: 5 W	4,450 mAh	186.2 × 133.8 × 6.3 mm^3	Natural convection. No information available.
LG wing	Oct 2020	Qualcomm Snapdragon 765G, TDP: 5 W	4,000 mAh	169.5 × 74.5 × 10.9 mm^3 (unrotated)	Natural convection. Thermal pad to phone chassis. Copper layer below the battery. No heat transfer across articulating joint.

a hinge region, and a vapour chamber extending from the first portion to the second portion across the hinge region, the vapour chamber comprising a first layer comprising titanium, a second layer comprising titanium joined to the first layer to form the vapour chamber, a working fluid within the vapour chamber, and a third layer comprising titanium positioned between the first layer and the second layer, the third layer comprising one or more features configured to conduct the working fluid via capillary action.". Microsoft [47,48] also filed patents that discussed a flexible thermal conduit that connects two sections of an electronic device similar in design to a virtual reality headset, transferring heat from a source to a heat-dissipating structure.

Dell [55] patented a dynamic system for thermal management for a foldable dual display device. The disclosure relates to active thermal management of a foldable "information handling device" with a passive cooling system.

Beyond foldable mobile electronic devices, flexible heat pipes find natural application when heat sources and heat sinks are not on the same plane. Examples of which include wearables for flexible thermal regulation devices [57], flexible and stretchable electronic systems for epidermal electronics [40], optical head-mounted devices [47], energy harvesting for Internet of things (IoT) wireless sensors [58], space [59,60] and aircraft [61] applications.

Non-flexible vapour chambers are an established technology [62,63]. They are traditionally constructed from rigid materials such as copper, aluminium, and stainless steel [64–66]. Recently, increasing research has been focused on ultra-thin [1,2,74–80,5,67–73] and flexible [64,81–84] heat pipes. However, research and development of flexible ultra-thin vapour chambers are limited [3,85–87]. There are no current high-performance ultra-thin, flexible heat pipe results for a 180° bend reported, as required for modern foldable mobile devices. This review endeavours to investigate and discuss the current state-of-the-art of ultra-thin flexible heat pipe technology. In tandem, promising manufacturing and internal cavity approaches (wicking structure and vapour space) are detailed for macroscale and ultra-thin rigid heat pipes. Ultra-thin rigid heat pipes are included as they are a precursor to their ultra-thin flexible counterparts with significant shared design components. This article will guide the development of flexible ultra-thin vapour chambers for the next generation of foldable mobile electronic devices.

2. Technology overview

Heat pipes are widely used in many industrial applications in the chemical, power generation, heating, ventilation, air conditioning, spacecraft, and aeronautical fields due to their high heat transfer coefficient [85]. They are most prominently implemented in the electronics industry to cool mobile devices, computers, radio frequency systems, high power light-emitting diodes, solar cells, and solid-state laser light sources [1,62,80]. Heat pipes possess particular advantages in temperature uniformity and local hot-spot elimination. They enable efficient transport of thermal energy by utilizing the latent heat associated with phase change [1,63,66] (see Fig. 1), with effective thermal conductivities that are an order of magnitude larger than their solid material counterparts [2].

A conventional heat pipe consists of an evaporator, condenser, wick, adiabatic section, and a working fluid. They are typically hermetically sealed from their surrounding environment, making them particularly attractive for use with electronic components. The inner chamber generally includes a porous metal layer or mesh, known as a wick, that facilitates liquid recirculation. In mobile electronics such as smartphones, heat is removed from the active component at the evaporator (CPU, heat source). At this location, the working fluid evaporates, carrying energy with it in the form of latent heat. This vapour diffuses through the heat pipe to the condenser (phone case, heat sink), where it changes phase back into liquid form. This condensed liquid is then transported back to the evaporator through the wick by capillary forces [85].

There are several variants of heat pipe technology, each with its preferred application cases. A traditional heat pipe transports heat in one direction, with an adiabatic section that connects the evaporator and condenser sections (Fig. 1a). Geometrically their width or diameter is significantly smaller than their length. They are typically constructed from flattened and sealed pipes using grooves, meshes, and sintered powder as wicking structures [67,71,75,86,87].

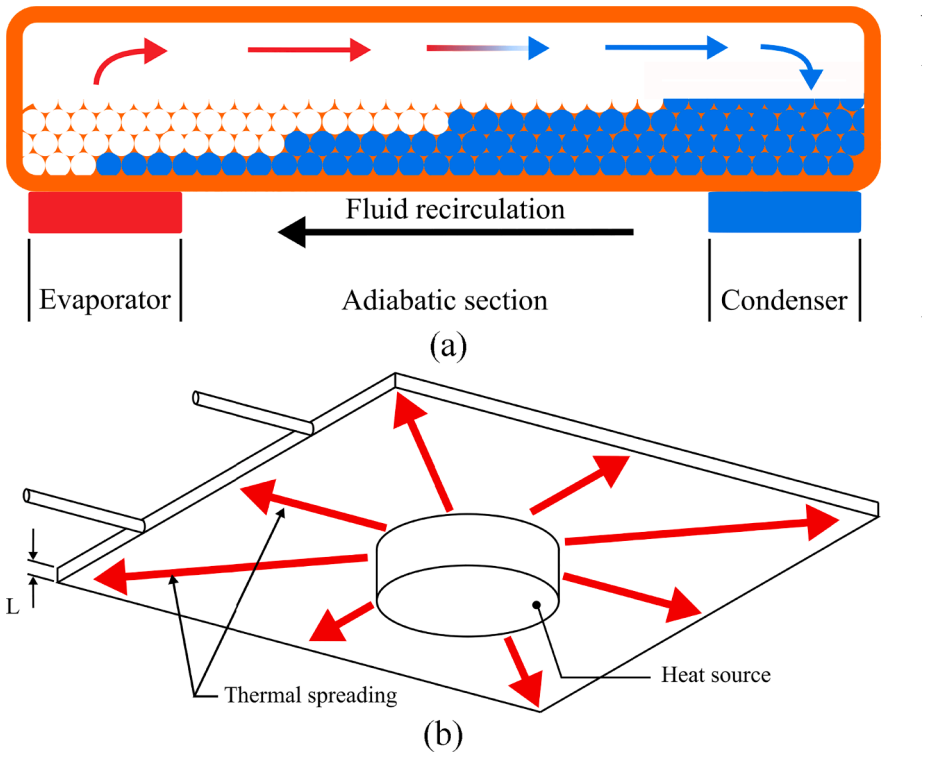

Fig. 1. Conventional (a) heat pipe and (b) vapour chamber operation.

A vapour chamber, flat plate heat pipe, or thermal spreader, as their name suggests, spread heat from a localized source in multiple directions (Fig. 1b). They are normally differentiated by the size of the condenser sections. For a vapour chamber, a localized heat source is spread across the entire surface, resulting in a much larger condenser section [88]. They are excellent candidates for electronic heat spreaders owing to their lightweight, geometric flexibility, and remarkably high thermal conductivity. This makes vapour chambers particularly suited to mobile device thermal dissipation, where the entire outer shell is utilized. However, while vapour chamber technology finds wide application in the cooling of high-power portable workstations such as the 2020 Dell XPS 17-9700 with a 10th generation Intel 45 W CPU and 55 W NVIDIA GPU [89]. The current state-of-the-art of the technology limits their implementation in smaller mobile devices.

Another prominent heat pipe technology for mobile electronics is a pulsating heat pipe. A pulsating heat pipe is made up of a long serpentine channel without any wick structure. The evaporator and condenser are located at the turns of the channels. Vapour bubbles grow in plugs from the evaporator and contract at the condenser. The plugs move between hot and cold areas creating an efficient convective heat exchange. The inner diameter of the serpentine channel must be sufficiently small to facilitating fluid movement [3,90]. While this research will primarily focus on wicked heat pipe technology, both pulsating heat pipes and traditional wicked heat pipes are intrinsically connected by their shell materials and it sealing and are included here.

A growing interest in ultra-thin heat pipe technology can be observed [1]. This article divides previous research into four categories, based on their thickness and flexibility. These are listed in Table 1. In tandem, promising manufacturing and internal cavity approaches (wicking structure and vapour space) are detailed for macroscale non-flexible heat pipes.

Heat pipe performance is strongly dependent on the wick's effectiveness to recirculate the working fluid from the condenser to the evaporator. A wick structure's performance is characterized by two critical parameters, permeability and capillarity [85,91]. Heat pipe wicks are traditionally constructed using woven wire meshes, metal foams, sintered powders, or advanced etching and coating techniques to the inner surfaces of the heat pipe chamber [74,75,77,85,92,93]. Wire meshes have been prominently employed as a wicking structure in ultra-thin flexible heat pipe applications due to their low cost, ductility, and ease of manufacturing [94–97]. Wire meshes are typically defined by their count number (#), which indicates the number of wires crossing per square inch.

The thermal characterization of a heat pipe generally consists of three approaches. These are shown in Fig. 2. The most common configuration is illustrated in Fig. 2a, where the heat pipe is heated and water-cooled at opposite ends. Thermal energy, in this case, moves in one direction. The next two cases are typically used in the characterization of vapour chambers, where the device is heated locally at the centre of its bottom surface and cooled on its top surface by water cooling, force convection (Fig. 2b) or natural convection (Fig. 2c). The heat in these cases moves in the lateral and vertical directions.

Three metrics are typically used to characterize heat pipe performance: (i) thermal conductivity, $k = \frac{qL}{\Delta TA}[W/(mK)]$, where q is the applied power, L is the length between temperature measurements, ΔT is the temperature difference across the characteristic length, and A is the cross-sectional area perpendicular to the direction of heat flow [6]. (ii) thermal resistance, $R = \Delta T/q$ [K/W], which characterises the temperature drop across the device for a given applied thermal power. It does not account for the geometry of the device [6]. (iii) dimensionless Coefficient of Thermal Spreading ($CTS = (T_{ave} - T_\infty)/(T_{max} - T_\infty)$) [8], where T_{ave} is the average surface temperature, T_∞ is the ambient farfield temperature, and T_{max} is the maximum surface temperature. CTS defines the effectiveness of heat spreading by accounting for the uniformity of the surface temperature. It can be calculated utilizing IR thermography or multiple local temperature measurements. It is an important metric for mobile electronics, which are typically cooled due to natural convection. A low-temperature uniformity indicates poor thermal spreading.

Considering the negative impact of a 1 °C temperature difference across a device for screen and battery performance [7,98–100], and using an average TDP (~ 5 W) value from Table 1, thermal management

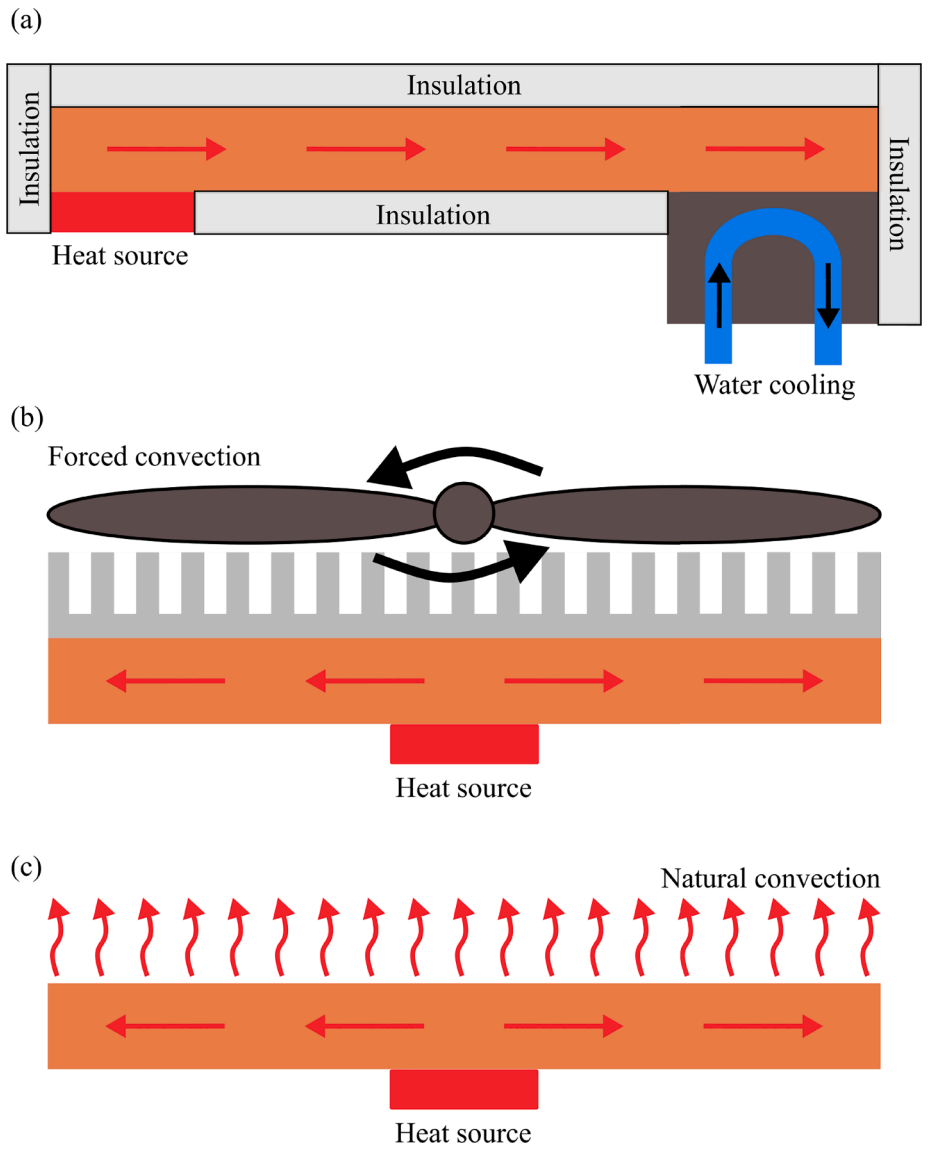

Fig. 2. Heat pipe thermal performance characterization methods. (a) liquid cooling, (b) forced convection, and (c) natural convection.

solutions for mobile electronics should target a thermal resistance of <0.2 K/W. With higher power devices requiring even lower thermal resistances. For context, a basic calculation using the above TDP and dimensions of a Galaxy Z Fold 2, assuming the max dimension as the characteristic length, shows that a ~16 mm thick solid copper spreader (k = 390 W/(m K)) would be required to maintain a 1 °C temperature difference across the device. This is 2.3 × thicker than the actual Galaxy Z Fold 2. To achieve the desired temperature difference across the device, for a small form factor (thickness, t < 1 mm), a thermal spreader with a thermal conductivity of >6,250 W/(m K) is required. Heat pipes are an ideal technology to achieve this.

Ultra-thin flexible heat pipe technology is an underdeveloped topic. It shares common design components with macro rigid, ultra-thin rigid, and macro flexible heat pipes. Ultra-thin flexible heat pipe design is a complex challenge incorporating evaporation, condensation, two-phase flow, flexible porous wick and flexible impermeable casing design all in a confined ultra-thin package. Future flexible heat pipe designs should incorporate the innovative advances made in these adjacent technologies. As such, select literature from these areas are included in this review to build a complete understanding of the current state-of-the-art and potential future development direction for ultra-thin flexible heat pipes.

2.1. Macro rigid heat pipes

This first section will focus on macro (thickness >2 mm) rigid heat pipes, focusing on novel fabrication and wicking approaches. Soloman et al. [101] investigated the deposition of copper nanoparticles (80–90 nm) on a 100 count copper mesh for a copper tube heat pipe (19.5 mm × 400 mm, ∅ × L) with water as the working fluid. The wick consisted of four mesh layers. The nanoparticles were deposited onto the wick by immersing the mesh into a copper particle nanofluid for 5 min and drying in 80 °C air. The procedure is repeated up to six times to produce the porous coating. The deposited nanoparticles are not detached from the wick by a normal water flush. A lower thermal resistance is noted in the evaporator for the coated wick compared to the uncoated case. However, a larger thermal resistance is noted in the condenser. The total resistance of heat pipe operated with a coated wick is lower than that of its uncoated counterpart for all applied heat inputs. It decreases with increasing heat input. A minimum heat pipe thermal resistance of ≈0.31 K/W is observed for the coated case at the maximum applied power of 200 W [101].

Wong et al. [102] fabricated and tested a rigid copper vapour chamber. Their device measured 100 mm × 90 mm, with no reported total thickness. Their internal liquid and vapour recirculation system

consisted of parallel triangular grooves of 1 mm spacing machined into the top plate and a composite wicking structure on the bottom plate consisting of a 100 and 200 count stacked meshes. The apex of the machined triangular groove was in direct contact with the composite mesh structure on the bottom section of the internal chamber. The grooves facilitated high permeability and provided an internal support structure. The heat pipe was tested for three heater sizes (1.21 cm^2, 4.41 cm^2, and 9.61 cm^2), working fluids (water, acetone, and methanol), one filling volume (3.4 mL), and a range of applied powers from 20 W to 460 W. The condenser area (89 cm^2) was kept constant for all tests. A minimum thermal resistance of ≈0.03 K/W was observed with water for the largest heater area and an applied power of 460 W [102].

Hsieh et al. [103] fabricated a flat plate heat pipe measuring 150.0 mm × 31.0 mm × 5.5 mm. The internal chamber consisted of three primary components; rectangular grooves (0.55 mm × 0.5 mm × 1 mm, depth × width × pitch), copper mesh layers (70 μm thick per layer), and a coronary stent support structure (1 mm thick) to optimize permeability and capillary pumping forces. The number of mesh layers was varied from no mesh to three mesh layers to investigate the impact on thermal resistance. Two heater sizes (1 cm^2 and 9.61 cm^2) and one condenser size (31 cm^2) were used during testing with acetone as the working fluid. The power input ranged from 20 W to 140 W. The most consistent performance across both heater sizes and applied powers were observed for the single mesh layer and microchannel configuration. A maximum power of 140 W was dissipated for grooves with no mesh at a ≈0.32 K/W for the 9.61 cm^2 heater size. A minimum thermal resistance of ≈0.11 K/W was achieved for the 1 cm^2 heater size with no mesh layers [103].

Wang et al. [104] experimentally investigated two different copper flat plate heat pipes with deionized water as the working fluid. Both plates measured 87 mm × 83 mm × 7 mm. The heat pipes were differentiated by their capillary structures, with intersected rectangular narrow grooves for the first flat plate heat pipes and interlaced circular channels for the second case. The grooves inside the first heat pipe are perpendicularly intersected, consisting of 37 longitudinal grooves and 38 transverse grooves on the bottom plate. Each groove has a rectangular cross-section (3 mm × 0.2 mm × 2.2 mm, height × width × spacing). The second heat pipe capillary structure was circular 1 mm interlaced channels with 3.5 mm spacing. The channels are drilled within the copper block (25 longitudinal and 24 transverse channels). The ends of each channel were sealed by welding to form the cavity space. The interlaced channels form the passageway for the working fluid and the vapour. An optimum thermal resistance of 0.183 K/W and 0.071 K/W was observed for first and second flat plate heat pipes at a filling ratio of 65% and 70%, respectively.

Sun and Qiu [105] designed an asymmetrical vapour chamber with a superhydrophilic evaporator to increase nucleation sites and a superhydrophobic condenser to increase dropwise condensation. The vapour chamber was 70 mm × 70 mm × 3 mm in size. It was heated locally on its bottom surface (2.25 cm^2) and cooled on its entire top surface. Its performance was compared with a bare sintered wick heat pipe. The thermal resistance in the vertical and horizontal directions was characterized. For a fixed applied heat flux, the asymmetrical vapour chamber was observed to generally outperform its bare sintered wick counterpart in both directions. However, at higher applied heat fluxes (>70 W/cm^2) in the horizontal direction, the conventional bare sintered wick outperformed its asymmetrical counterpart. A minimal thermal resistance of ≈0.31 K/W and ≈0.06 K/W was observed for the asymmetrical vapour chamber at an applied power of 207 W in the vertical and horizontal directions, respectively [105].

Peng et al. [107] investigated a nature-based leaf vein system wick for vapour chamber applications. The wick is manufactured by chemical etching copper to produce the desired structure. The deepest channel is almost 0.3 mm, and the channel width decreases as the wicking structure increases in radial distance from the centre. The designed vapour chamber was 90 mm in diameter and varied height. Three vapour chamber combinations were investigated with brass and copper as the base materials and several applied powers (10 W–90 W). A maximum power of 90 W was dissipated for the copper leaf vein system wick evaporator and a plain copper substrate condenser. A thermal resistance of ≈0.17 K/W was observed in this case with water as the working fluid [107]. The authors noted that the performance was limited due to the lack of wicking structure on the vapour chamber vertical walls. As a result, the working fluid can only flow back to the evaporator by gravity.

Dai et al. [106] explored micromembrane-enhanced evaporating surfaces to enhance capillary evaporation for water with application in ultra-thin heat pipe technology (Fig. 3). Four substrates were investigated: copper microchannels (250 μm × 250 μm, width × height, wall thickness: 250 μm), single layer copper mesh screen (thickness: 80 μm), four-layer sintered copper mesh screens (thickness: 320 μm), and the micromembrane-enhanced evaporating surfaces (total thickness of sintered microchannels and mesh: 320 μm). For the micromembrane, the copper mesh screen was diffusion bonded on microchannels to promote capillary pressure and reduce flow resistance effectively. Compared with mono-porous evaporating surfaces such as microchannels and copper mesh laminates of similar thickness and working conditions, the critical heat flux was substantially increased by 83% and 198%, respectively. This was due to the separation of the capillary pressure generation and fluid transport process that was enabled by the micromembrane. Oscillating flows induced by the bubble growth and collapse as well as the capillary flows induced by the receding menisci were observed and believed to play important roles in enhancing the heat transfer by

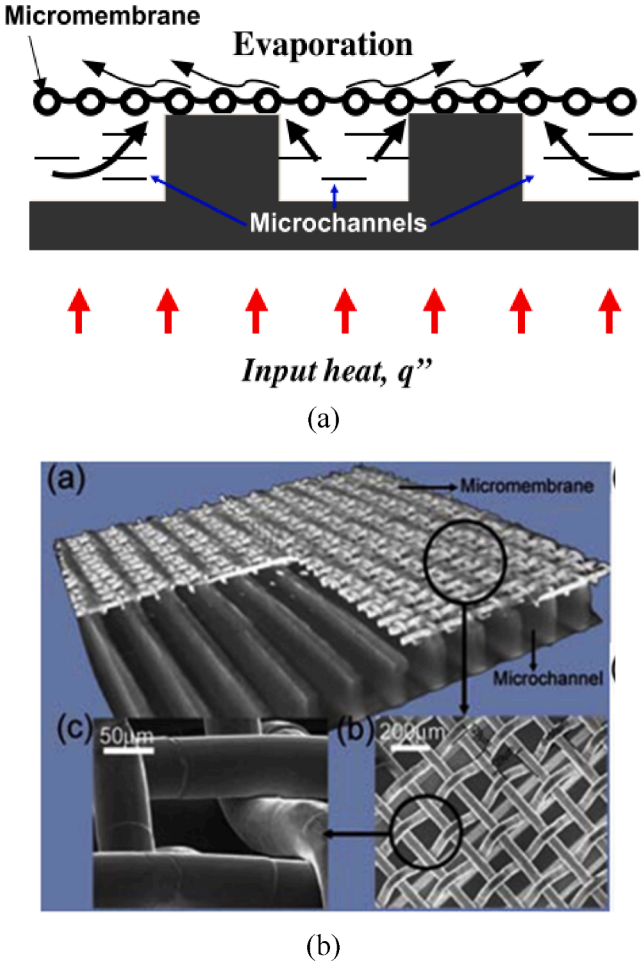

Fig. 3. (a) Design of micromembrane-enhanced evaporating surfaces, and (b) three dimensional (3D) Micro-XCT image of the micromembrane-enhanced evaporating surface [106].

inducing advection and improving evaporation and nucleate boiling.

Shaeria et al. [108] investigated a vapour chamber combining hydrophobic and hydrophilic wettability conditions in the evaporator to optimize thermal performance. The proposed vapour chamber was 76.2 mm × 76.2 mm × 3.5 mm, included a separate layer of hydrophilic sintered copper powder wick that was pressed in intimate contact with a hydrophobic evaporator substrate with a water contact angle of 140°. Shaeria et al. stipulated that this configuration used the hydrophilic wick to force liquid in contact with a hydrophobic evaporating surface. The contact between the wicking layer and the evaporator was provided by sixteen posts implemented on the condenser side, which compressed the wicking layer toward the evaporator. The vapour chamber was centrally heated (9.4 cm^2) from the bottom and cooled on its entire top surface. Water was used as the working fluid, with five filling ratios (14%–27%) and a range of applied heat fluxes (40 W/cm^2–215 W/cm^2) explored. Results were compared with those of a baseline vapour chamber fabricated by sintering hydrophilic copper particles on a hydrophilic copper evaporator substrate. Overall, the proposed vapour chamber's thermal resistance was larger than that of the baseline vapour chamber. This was possibly due to insufficient mechanical contacts between the wicking layer and the hydrophobic evaporator, which may have confined the outward vapour and inward liquid in the microscale gaps between the wicking layer and the hydrophobic evaporator. A maximum reported thermal power of ≈150 W was dissipated for a total thermal resistance of ≈0.37 K/W at a filling ratio of 18%. Under the same applied power and filling ratio, the baseline vapour chamber had a total thermal resistance of ≈0.15 K/W [108].

Deng et al. [109] fabricated ten copper composite porous vapour chambers measuring 75 mm × 75 mm × 6 mm with ethanol as the working fluid. The evaporator and condenser wick for all vapour chambers were constructed from porous sintered copper particles and sintered to the top and bottom internal plates. The evaporator (63 mm × 63 mm × 2.5 mm) had 16 uniform radial grooves, providing fast liquid backflow with low hydraulic resistance, while the condenser consisted of a continuous porous structure (63 mm × 63 mm × 0.5 mm). The evaporator and condenser wicks were in direct contact providing structural support. The ten different vapour chambers consisted of five different particle sizes ranging fro <50 μm–150 μm for spherical and irregular particle shapes. After sintering, the top and bottom plates were welded together by braze welding under pressure and a protecting atmosphere. A 40% filling ratio was implemented for all tests. Generally, the spherical particle outperformed their irregular counterparts. The vapour chamber with a spherical powder size of 50 μm–75 μm had the lowest thermal resistance of ≈0.15 K/W for a range of power input from 50 W to 280 W [109].

Feng et al. [85] constructed an ultra-large, copper flat plate heat pipe (180 mm × 180 mm × 3 mm) using thermal spraying and water as the working fluid (Fig. 4). The porous copper wick was fabricated using a flame spray torch to deposit a mixture of copper and aluminium particles onto the target substrate. A stainless-steel wire mesh acts as a mask so that the deposited coating is in the form of an array of microstructures with channels between them. After spraying, the aluminium deposit is leached away by immersing the plate in a dilute NaOH solution to produce a porous structure. The heat pipe was sealed using vacuum brazing and had an internal cavity of 176 mm × 176 mm × 1 mm. The heat pipe was centrally heated from its bottom and cooled along its top outer edge. The heat pipe was tested horizontally for three filling ratios (35%, 50%, and 65%), six applied power levels (33 W–200 W) and contrasted with a solid copper sheet of the same dimensions. A peak average radial thermal conductivity of 920 W/(m K) and a thermal resistance of 0.05 K/W was noted for a 65% filling ratio and 7.5 W/cm^2 applied heat flux.

A summary of the key heat pipe characteristics in Section 2.1 are shown in Table 3. When compiling the data, horizontal, non-gravity assisted data was included preferentially to allow a fair comparison between studies. For the operating temperature range, if the heat pipe temperature data is not presented, the coolant temperature is used for the lower temperature range. The upper temperature is calculated using the heat pipe thermal resistance and applied power. For thermal conductivity calculations, the external cross-sectional area is used, and if not quoted or easily discernible, the length of the heat pipe is used for the effective length. In cases where magnitudes are not directly quoted in the paper, the best estimates are provided by the authors. Thus, the magnitudes presented in this review serve only as an approximation for performance comparison purposes. The most common keywords for these works are vapour chamber (× 6), thermal resistance (× 4), and heat pipe (× 3).

In the contexts of flexible heat pipe technology for foldable electronic devices, due to the reduced heat pipe thickness and subsequent internal cavity spacing, the augmentation of wettability, similar to Soloman et al. [101], Sun and Qiu [105] and Shaeria et al. [108], is a sensible approach to optimise the pumping power and heat transfer performance of the evaporator and condenser. Although not directly applicable to flexible heat pipe technology given their rigid characteristics, the multi-scale porous structures shown by Peng et al. [107], Deng et al. [109], Feng et al. [85] to optimise fluid recirculation and vapour movement in the

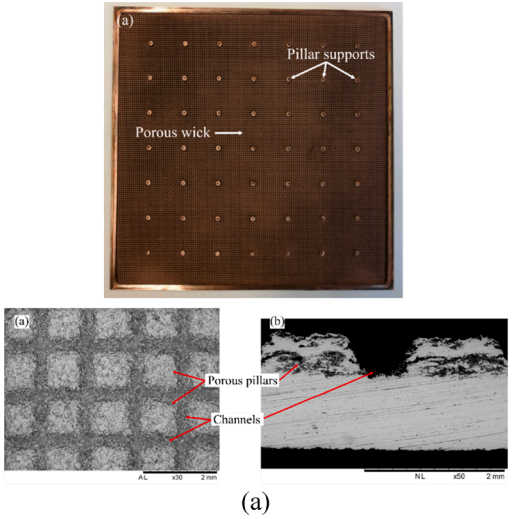

(a)

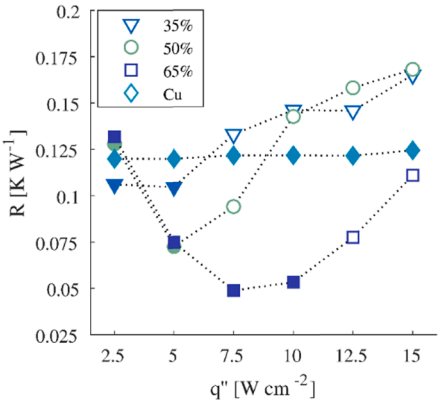

(b)

Fig. 4. (a) Top view of structured porous copper coating, an SEM cross-section view of structured porous copper coating, and (b) average radial thermal resistance for varied applied heat flux and filling ratio. Filled markers denote non-dry out condition. Empty markers represent when dry out has occurred [85].

Table 3
Macro rigid heat pipe summary.

Ref	Year	Type	Base material	Dimension	Wick	Working fluid	Orientation	Gravity assisted	Cooling medium	Operating temperature range [°C]	Power [W]	Thermal resistance [K/W]	Thermal conductivity [W/m K]
Soloman et al. [101]	2012	round, rigid	copper	19.5 mm × 400 mm (⌀ × L)	copper nanoparticles coated mesh, 4 layer (#100)	water	horizontal	no	Water, forced convection	42–116	200	0.31	2.1×10^3
Wong et al. [102]	2011	flat, rigid	copper	100 mm × 90 mm × 1.34 mm (L × W × H)	copper triangular grooves and mesh, 2 layer (#100 + 200)	Water, methanol and acetone	horizontal	no	Air, forced convection	NA	460	0.03	N/A
Hsieh et al. [103]	2012	flat, rigid	aluminium	150 mm × 31 mm × 5.5 mm (L × W × H)	aluminium rectangular channels and mesh,	acetone	horizontal	no	Coolant, forced convection	50–62.5	140	0.32	2×10^3
Wang et al. [104]	2013	flat, rigid	copper	87 mm × 83 mm × 7 mm (L × W × H)	copper circular channels,	water	horizontal	no	Air, forced convection	98–93	~30	0.07	N/A
Sun et al. [105]	2014	flat, rigid	copper	70 mm × 70 mm × 3 mm (L × W × H)	copper powder, sintered	water and ethanol	horizontal	no	Water, forced convection	35–100	207	0.10	N/A
Peng et al. [107]	2015	flat, rigid	copper	90 mm × N/A mm (⌀ × L)	copper etched channels, leaf-vein-like fractal network	water and ethanol	horizontal	no	Air, forced convection	N/A	90	0.17	N/A
Shaeri et al. [108]	2017	flat, rigid	copper	76.2 mm × 76.2 mm × 3.5 mm (L × W × H)	copper powder, sintered	water	horizontal	no	Water, forced convection	48–105	152	0.37	N/A
Deng et al. [109]	2017	flat, rigid	copper	75 mm × 75 mm × 6 mm (L × W × H)	copper powder, sintered	ethanol	horizontal	no	Water, forced convection	30–40	280	0.14	N/A
Feng et al. [85]	2020	flat, rigid	copper	180 mm × 180 mm × 3 mm (L × W × H)	copper porous frustums and triangular channels, thermal spray	water	horizontal	no	Water, forced convection	48–55	100	0.05	920

cavity are important results. The principles shown can be applied to the flexible wick structure of a flexible heat pipe to optimise two-phase flow and phase change in the internal cavity.

2.2. Ultra-thin heat pipes

2.2.1. Ultra-thin heat pipe design methodology

Yadavalli et al. [2] analytically and numerically explored ultra-thin heat pipe performance limitations. A thermal resistance network model and a detailed 2-D numerical model were used to analyse heat pipes' performance under varied conditions. A broad parametric study of geometries and heat inputs using the reduced-order model delineated the heat pipe performance thresholds. A vapour-phase threshold unique to ultra-thin heat pipes operating at low-power inputs is observed. At this threshold, the vapour-phase thermal resistance imposed by the saturation pressure/temperature gradient in the heat pipe causes a crossover in the thermal resistance relative to a solid heat spreader. The higher fidelity numerical model is used to assess the accuracy of the resistance network model and verify each assumption's validity and applicability regarding the transport mechanisms. Key heat transfer mechanisms not captured by the reduced-order thermal network models are identified. These include the effects of boundary conditions on the interface mass flux profile, convective effects on the vapour core temperature drop, and 2-D conduction on smearing of evaporation/condensation mass flux into the adiabatic section.

Patankar et al. [5] developed a design methodology for vapour chambers to yield improved condenser-side temperature uniformity at ultra-thin form factors in mobile device applications. A biporous condenser-side wick design is proposed that facilitates a thicker vapour core, reducing the condenser surface peak-to-mean temperature difference by 37% relative to a monolithic wick structure. Patankar et al. concluded that the layout of the condenser-side wick governs condenser-surface temperature uniformity. Temperature uniformity can be improved by increasing thermal resistance across the condenser-side wick in the heat input region and increasing condenser-side wick permeability to reduce its thickness and increase the vapour-core thickness for lowered lateral thermal resistance.

Patankar et al. [68] explored working fluid selection for ultra-thin vapour chambers. A resistance-network-based model is used to develop a simple analytical relationship for the vapour chamber thermal resistance as a function of the working fluid properties, operating power, and geometry. Six working fluids were investigated (Acetone, Methanol Water, Pentane, Ethanol, and R141b). Their model had a thermal performance objective instead of a maximized power dissipation capability. A working fluid is sought in this case that provides a minimal thermal resistance while ensuring a capillary limit is not reached at the target operating power. They observed that at small thicknesses, the thermal resistance of vapour chambers becomes governed by the saturation temperature gradient in the vapour core, dependent on the working fluid's thermophysical properties. The working fluid choice cannot be based on a single figure of merit containing only fluid properties to satisfy the performance objective. Instead, the functional relationship for thermal resistance must be analyzed, taking into account all operating and geometric parameters, in addition to the thermophysical fluid properties.

Patankar et al. [69] investigated a thin vapour chamber's transient thermal behaviour using a low-cost 3D, transient semi-analytical transport model. They identified three key mechanisms that govern the transient thermal response: (i) the total thermal capacity of the vapour chamber governs the rate of increase of the volume-averaged mean temperature; (ii) the effective in-plane diffusivity governs the time required for the spatial temperature profile to initially develop; and (iii) the effective in-plane conductance of the vapour core governs the range of the spatial temperature variation, and by extension, the steady-state performance.

Huang et al. [70] explored the relationship between the thickness and width of the vapour flow path of an ultra-thin vapour chamber. They developed a relationship to relate the Poiseuille number of a rectangular micro-channel to vapour channel thickness and width. When the thickness of the vapour flow path is less than 0.3 mm or the width is less than 2 mm, their relationship increased rapidly. They noted that a greater influence of the support type on the vapour pressure drop is observed for lower vapour path thicknesses. Reducing the support columns' diameter and spacing is a good way to balance the support effect and vapour pressure drop. The sequential arrangement had a smaller pressure drop than the cross arrangement, with circular supports having the lowest associated pressure drop. They determined that a spaced wick structure approach was more suitable for ultra-thin vapour chambers than a layered approach.

2.2.2. Flattened ultra-thin heat pipe

Aoki et al. [86] developed two ultra-thin flattened heat pipes of varied sizes. The first heat pipe measured 150 mm × 9 mm × 1 mm, while the second measured 100 mm × 9 mm × 0.7 mm. Both flattened heat pipes utilized a hydrophilically treated (oxidation–reduction process) copper mesh as the wicking structure and water as the working fluid. The heat pipes were tested for a range of applied powers (2 W–25 W) and tilt angle (0°–90°), with the evaporator maintained above the condenser for all tilt angles. The authors demonstrated a thermal power transfer of 20 W and thermal resistance of 0.2 K/W for the 1 mm thick heat pipe and 7 W thermal transfer for a thermal resistance of 0.4 K/W for the 0.7 mm thick heat pipe.

Li et al. [67] compared three different composite wick structures for flattened ultra-thin heat pipes. The heat pipes measured 200 mm × 7.8 mm × 1 mm with water as the working fluid. The first heat pipe had a sintered powder wick on one surface of the internal cavity, the second had a sintered wick on both the top and bottom surfaces, and the final had a mesh sintered to the top and bottom surfaces. Deformation of the three wicking structures was noted due to the flattening process. The capillary limit was found to be the primary heat transfer limit. The three heat pipes were tested for varied filling ratios (50%–80%) and applied power (8 W–15 W) in the horizontal orientation. An optimum filling ratio of 70%, 70%, and 80% was observed, respectively. A maximum thermal power dissipation of 12 W, 13 W, and 14 W for the optimum filling ratio and a calculated total thermal resistance of ≈0.29 K/W, ≈0.51 K/W, and ≈0.4 K/W were observed, respectively.

Yang et al. [71] considered an ultra-thin flattened heat pipe with a braided copper composite wire wick structure. The flattened heat pipe was 100 mm × 9.1 mm × 1 mm in size, and deionized water was used as the working fluid. Yang et al. explored two wick structures; the first was composite braided wire, using a large diameter (0.1 mm) in the core, while the exterior of the core is covered by smaller diameter copper wires (0.05 mm). The second was a mono braided wick structure with 0.1 mm wires. Both wicks were hydrophilically treated by oxidizing their surface to increase wettability. Both flattened heat pipes were tested for varied filling loading ratios (103%–142%), applied power (10 W–24 W), and tilt angle (−60° to +60°). Yang et al. defined their filling ratio as the volume of filled working fluid divided by the empty space in the wicking structure. The composite design outperformed the mono design by more than 32.5% in all orientations. An optimum filling loading ratio of 125% yielded the lowest thermal resistance of 0.12 K/W for a heat transfer capability of 20 W.

Zhou et al. [75] created a composite ultra-thin heat pipe by flattening a copper cylindrical heat pipe with an initial outer diameter of 2 mm (Fig. 5). The flattened heat pipe was 100 mm × 2.7 mm × 0.8 mm. The composite wick structure is made of a composite sintered copper foam and mesh wick. The wick is fabricated by sintering 0.3 mm thick copper foam to a 0.1 mm copper mesh. The authors stipulate that the copper foam wick has the advantages of high porosity and large capillary force, while the mesh wick is easy to bend and has high mechanical strength. The flattened heat pipe was tested for varied filling ratios (57%–115%) and applied power (2.5 W–5 W) in the horizontal orientation, where the

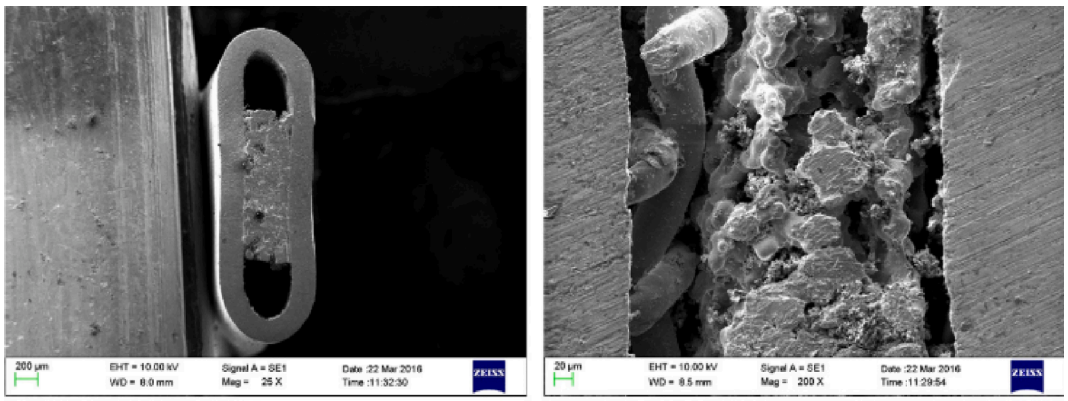

Fig. 5. SEM photographs of ultra-thin heat pipe: (a) cross-section and (b) partial magnification [75].

filling ratio was defined similarly to Yang et al. [71]. A maximum power of 5 W was sustained at a filling ratio of 100%, resulting in a thermal resistance of 0.74 K/W.

Zhou et al. [72] investigated a biporous spiral woven mesh wick for copper fattened heat pipes. The heat pipe was 120 mm × 7.7 mm × 1.1 mm in size. The biporous spiral woven mesh consisted of two layers woven using a varied ratio of 0.05 and 0.04 mm (OD) copper wires per layer. The performance was contrasted with a monoporous three-layer spiral woven mesh. The flattened heat pipe was tested for varied filling ratios (80%–140%) and applied power (10 W–26 W) in the horizontal orientation with water as the working fluid. The filling ratio was defined similarly to Yang et al. [71]. Testing showed that the optimal wick configuration was the monoporous three-layer spiral woven mesh over the biporous counterparts. A maximum heat transport of 18 W, 24 W, and 26 W, for a total thermal resistance of 0.136 K/W, 0.101 K/W, and 0.092 K/W was achieved for the two biporous cases and monoporous cases, respectively.

Zhou et al. [87] explored the impact of liquid to vapour space ratio on the heat transfer performance for flattened thin heat pipes (120 mm × 9 mm × 0.75 mm) with water as the working fluid. The wicks of various widths (2 mm–7 mm) consisted of two-layer sintered 100 count and 180 count copper mesh. Each heat pipe was characterized for several applied powers (2 W–8.5 W) and filling ratios (80%–140% (of the wick pore volume). A decreasing optimum filling ratio was noted for increasing wick width (wick pore volume). An optimum wick width of 4 mm with a filling ratio of 120% was observed to transfer 8.5 W.

Zhang et al. [80] proposed an aluminium flattened heat pipe that was 26 mm × 1.5 mm × 200 mm in size and used acetone as the working fluid. The extruded aluminium tube contains four separate cavities that work as independent micro heat pipes. Seven wick conditions were characterized; a smooth wickless heat pipe, three sintered aluminium fibres of varied porosity (150 µm wire diameter, ε = 70%, 75%, and 80%) and three commercial meshes with varied corrosion time (120 µm, 87 µm and 72 µm wire diameter, ε = 55.8%, 71.7%, and 77.3%). The heat pipes were tested for varied applied power (10 W–26 W), and three inclination angles (90°, 60°, and 30°), with the condenser always maintained above the evaporator, aiding fluid recirculation due to gravity. The smooth wickless ultra-thin heat pipe achieved the lowest total thermal resistance of ≈0.04 K/W at 30 W in the vertical orientation compared to all wick-based heat pipes. However, the commercial aluminium mesh (87 µm wire diameter, ε = 71.7%) demonstrated the best thermal performance of 0.13 K/W at 25 W at the smallest inclination angle (30°) due to sufficient liquid replenishment to the evaporator by the porous wick.

2.2.3. *Ultra-thin flat plate heat pipe*

Ivanova et al. [110] developed a thin flat silicon heat pipe (50 mm × 50 mm × 1 mm) utilizing discrete hexagonal pins in the evaporator, radial grooves in the adiabatic section, and rectangular grooves in the condenser using deep plasma etching. The heat pipe was thermal annealing under inert gas to seal the silicon wafers together. It was centrally heated and cooled around its outer edges for a constant filling volume (650 µL) using water as the working fluid. The heat pipe was tested for varied applied power (5 W–75 W) in the horizontal orientation and demonstrated a thermal resistance of 0.9 K/W for an applied power of 75 W.

Ding et al. [93] characterized a Titanium-based heat pipe (30 mm × 30 mm × 0.6 mm) with water as the working fluid. The wicking structure consisted of an array of deep-etched Titanium pillars (5 µm × 50 µm × 10 µm, diameter × height × pitch) that were hydrophilically treated by oxidization to create ~200 nm nanostructured titania on the pillar surfaces. The Titanium heat pipe was sealed using pulsed laser welding and charged with sufficient water to fill the pores up to the top of the pillars. Testing consisted of four applied powers (4 W–7.2 W), with heat transferred laterally through the heat pipe to opposite edges, in the horizontal orientation. A minimum thermal resistance of 2.69 K/W at 7.2 W was reported.

Oshman et al. [79] created a polymer-based flat heat pipe of 60 mm × 30 mm, with an internal vapour core thickness of 1 mm. Liquid-crystal polymer films (0.1 mm thick) with copper-filled thermal vias and a glass slide are employed as the case material. A copper micropillar (200 µm × 200 µm × 80 µm, W × L × H) and copper woven mesh (#200) hybrid structure were implemented for the wick, and water was selected as the working fluid. The microchannels for liquid transport are formed by first electroplating the bottom copper layer from 18 to 100 µm and then using photolithography and wet etching to define the pillars. Rather than channels, pillars are chosen to allow the liquid to return to the evaporator from any direction and achieve uniform liquid distribution in the evaporating area. A single layer of woven copper mesh is then pressed uniformly to the top of the formed pillars and then bonded by electroplating to create a hybrid wicking structure. A 20 µm layer of copper remains to line the inside of the polymer-based flat heat pipe to serve as a gas and liquid diffusion barrier due to the low permeability of liquid–crystal polymer films. The heat pipe was tested for a varied applied power (2.85 W–11.94 W), tilt angle (−90° to +90°), and a fixed filling volume of 0.198 mL of water. The heat pipe can operate for a heat flux of 11.94 W/cm^2 with a thermal resistance of 1.11 K/W and a reported effective thermal conductivity of 650 W/(m K). A minimal thermal resistance of 0.92 K/W is noted for the minimum applied power of 2.85 W. A reliability test of the heat pipe shows its performance degraded with time. The performance degradation was attributed to the gradual generation of a small quantity of noncondensing gas or the partial flooding of the condensation area, which would increase the thermal resistance on the condenser side.

Lewis et al. [78] constructed an ultra-thin heat pipe using polymer materials (Fig. 6). The heat pipe measured 60 mm × 20 mm × 0.3 mm. Polyimide was employed as the casing material, while micropatterned SU-8 provided both a liquid wicking structure and pillars to support the casing over a vapour core. An ultra-thin TiO2 film was deposited over the SU-8 and Kapton via atomic layer deposition, which acted as both a moisture barrier and a hydrophilic coating on the polymer surfaces. The coated polymer layers were sealed together using FEP. The heat pipe was tested for varied applied power (≈1.5 W–9.54 W) and a fixed filling volume of 0.15 mL of water in the horizontal orientation [78]. The lowest thermal resistance of 11.92 K/W occurred at 9.54 W, 73.1% of the reference copper, giving the polymer heat pipe an effective thermal conductivity of 541 W/(m K). The heat pipe's final mass was 0.85 g, a factor of four lower than an equally sized copper heat spreader.

Yang et al. [111] explored a flat polymer heat pipe (40 mm × 35 mm × 2 mm) with embedded copper thermal vias (0.5 mm diameter) to enhance thermal conductivity through the FR4 shell (Fig. 7). The heat pipe consists of a copper frame (1 mm thick), sandwiched between the top and bottom sheets of FR4 polymer to form a vapour chamber and

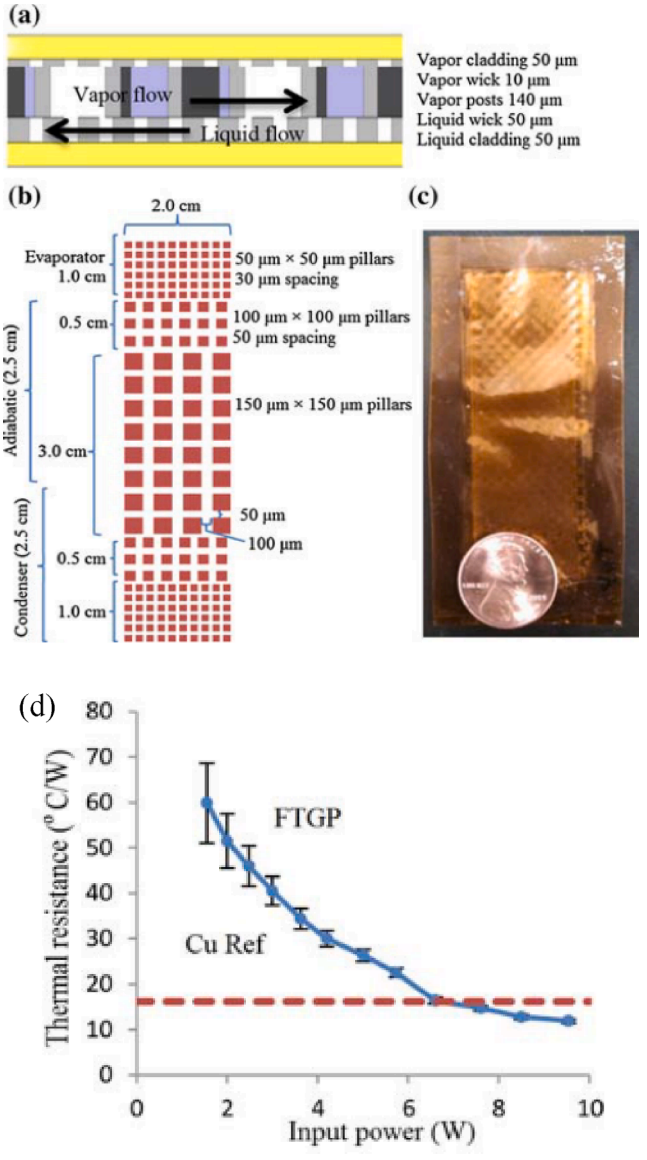

Fig. 6. (a) Cross-sectional schematics of the ultra-thin polymer heat pipe, (b) top-view schematic of the micropillar wick, (c) photograph of the complete polymer heat pipe, and (d) measured thermal resistance of polymer heat pipe (dots/solid line) and copper (dashed line) [78].

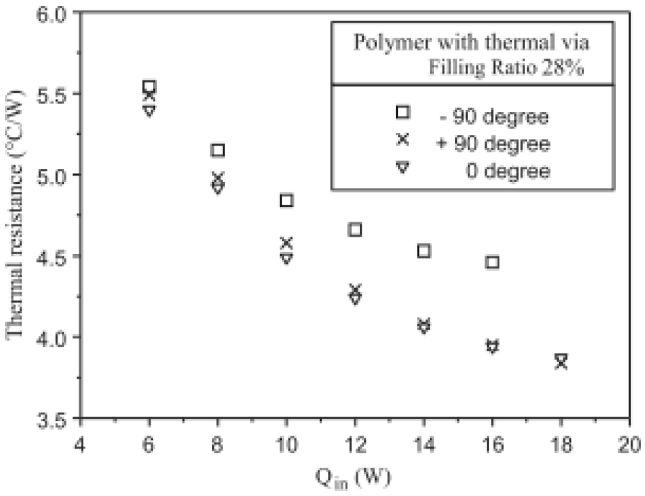

Fig. 7. Thermal resistance of a flat heat pipe with thermal via at different orientations: heat pipe horizontal (0°), heat pipe vertical (+90) with evaporator at the bottom, heat pipe vertical with the condenser at the bottom (−90°) [111].

used water as the working fluid. Two layers of copper mesh 200 count (50 μm wire diameter) and 100 count (115 μm wire diameter) formed the wick structure on the top and bottom interior surface, respectively. The heat pipe was sealed by applying a low-temperature solder in a vacuum drying chamber. The produced heat pipe was compared to an identical counterpart that did not possess the thermal via design. Testing consisted of varied applied power (6 W–35 W), filling ratio (0%–41%), and three tilt angles (-90° to + 90°). The thermal via design reduced the calculated thermal resistance by 20–25%. In the horizontal orientation, a minimum thermal resistance of 3.84 K/W was noted for a filling ratio of 28% and an applied power of 18 W.

Chang et al. [76] developed a loop-type vapour chamber of internal dimensions 110 mm × 50 mm × 0.5 mm (Fig. 8). The evaporator and condenser are respectively configured as multiple parallel channels and a pin–fin jointed chamber. The interconnected multiple evaporator channels are constructed by a series of 0.5 × 0.5 mm^2 square-sectioned ribs, whereas the diameter of each jointed pin–fin in the condenser chamber is 3 mm. The evaporator capillary structure consists of 0.05 mm deep square-sectioned parallel and staggered grooves at the same pitch of 0.05 mm are machined over the 3 mm thick heating endwall using a laser beam. With the various capillary (grooved) structures over the condenser and evaporator endwalls, an additional mesh composed of the copper wire mesh (0.01 mm wire diameter and 0.05 mm wire spacing) is laid above the 0.05 mm deep imprints over the evaporator

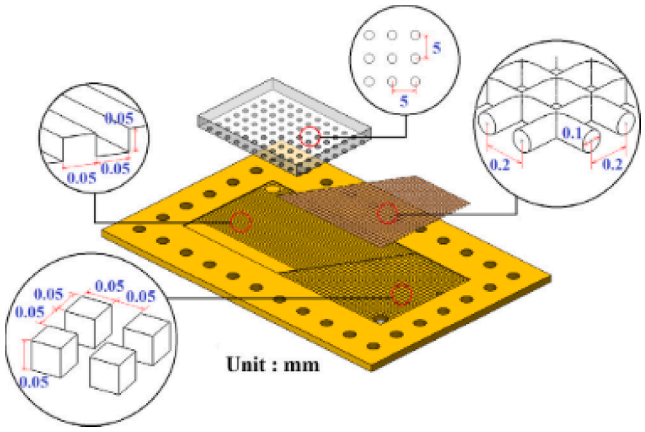

Fig. 8. Capillary structure of the loop-type vapour chamber [76].

endwall. The loop-type vapour chamber was testing in both the horizontal and vertical orientation for varied applied power (15 W–30 W) and water as the working fluid at a 50% filling ratio. The loop-type vapour chamber was outperformed by its solid copper counterpart in both vertical and horizontal orientations for thermal resistance.

Li et al. [74] characterized a thin copper flat heat pipe (100 mm × 50 mm × 2 mm) composed of a novel wick structure with an inner thickness of 1 mm and water as the working fluid (Fig. 9). The wick structure was made of sintered hybrid copper fine powder with diameters ranging from 50 μm to 100 μm (30/70 by weight). Their wick structure incorporated alternating channels for liquid and vapour transport. The heat pipe was tested for a varied applied power (12 W–120 W), five inclination angles (from −90° to + 90°), and a 45% filling ratio. Results showed that the proposed flat heat pipe could effectively dissipate 120 W (100 W/cm^2) in the horizontal orientation with a thermal resistance of 0.196 K/W.

Lv and Li [77] developed an ultra-thin flat copper heat pipe with dimensions 100 mm × 50 mm × 0.95 mm and deionized water as the working fluid (Fig. 10). To maximize the capillary force, a five-layer staggered arranged superhydrophilic copper mesh (#150) with a total thickness of 0.6 mm was fabricated by a unique etching and sintering combined process. Rectangular-shaped channels are directly machined through the mesh, forming an array of channels as well as striped wick structures. The machined channels function as vapour flow passages. The formed strip-shaped wick for condensate flowing back to the heating section, can significantly weaken the interaction between the vapour and the condensate. The heat pipe was tested for a single heater configuration for an applied power of 9 W–49 W and a filling ratio of 51% in the horizontal orientation. The heat pipe could dissipate 49 W (490 W/cm^2) without dry-out at a thermal resistance of 1.03 W/K. A minimum thermal resistance of 0.39 W/K was noted for an applied power of 30.25 W.

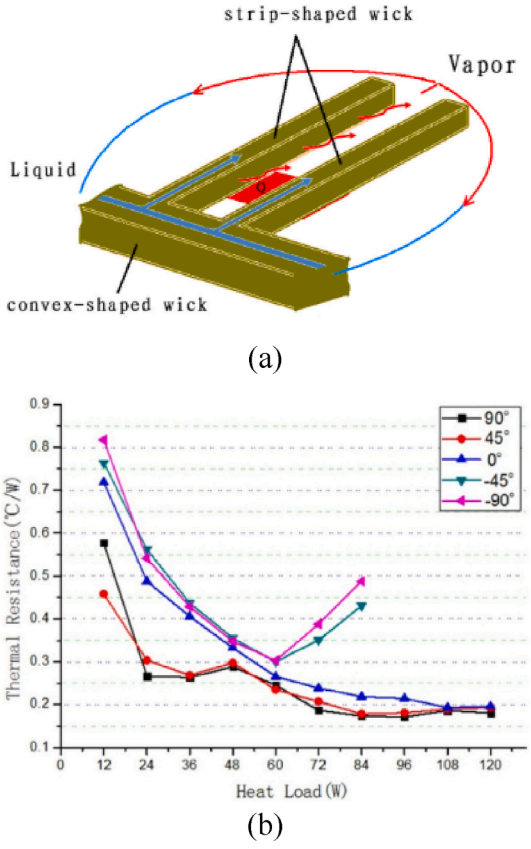

Fig. 9. (a) Flat heat pipe schematic working mechanism, and (b) thermal resistance of the flat heat pipe under different tilt angles [74].

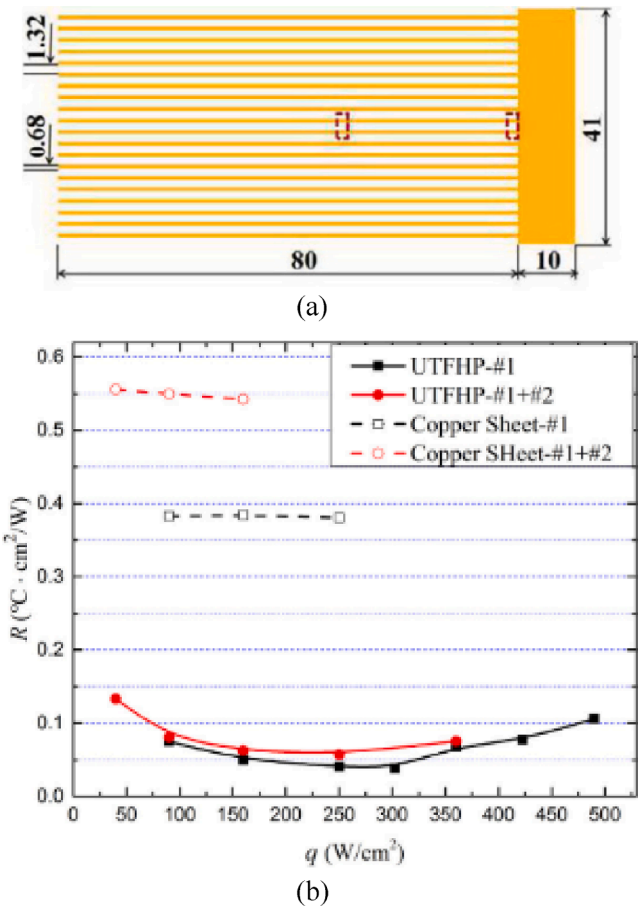

Fig. 10. (a) Dimensions of the wick structure, and (b) thermal performance measured by IR camera, thermal spreading resistance [77].

In their follow on work, Li et al. [112] visually investigated the two-phase flow characteristics of a similar wick geometry. They noted that their superhydrophilically treated (hydrochloric acid and sintering) wicking and vapour structure functioned well to regulate two-phase flow, alleviating the two-phase counterflow. Later, an ultra-thin heat pipe was developed (100 m × 50 mm × 0.5 mm) using 100 μm thick copper foil for the casing and a 300 μm thick multi-layer wick (#150) with alternating wick and vapour channels. The heat pipe was tested under natural convection cooling on the top surface, two heater sizes (6.25 cm^2 cm and 1.35 cm^2), for varied power input (2 W–10 W), tilt angles (from −90° to + 90°), and filling ratios (25.3%–56.8%). An effective in-plane thermal conductivity of 2.8 × 10^3 W/(m·K) at 7.37 W was reported for the largest heater size and a 44.2% filling ratio in the horizontal orientation.

Chen et al. [73] constructed and tested a thin aluminium flat plate heat pipe (120 mm × 120 mm × 2 mm) and acetone as the working fluid. An evaporator container with support posts and a filling hole was manufactured by a stamping method. The surface-functional wicks were fabricated by a micro-milling method, consisting of an array of orthogonal triangular microgrooves. The groove surfaces were covered with grain-like microstructures, enhancing hydrophilicity. The heat pipe was tested for a varied applied power (60 W–100 W), four inclination angles (0°, 30°, 60°, and 90°), and a 40% filling ratio. The results showed that the heat pipe could effectively dissipate 160 W at a thermal resistance of 0.16 K/W in the horizontal orientation.

Huang et al. [91] investigated five copper-based thin heat pipe designs (100 mm × 65 mm × 1.26–1.77 mm) with water as the working fluid. The five iterations consisted of two fine copper meshes (#100 and #200) as a wick and three copper coarse meshes (#12, #16, and #20)

for structural support. All configuration consisted of two sintered fine layer meshes (consistent size) with one coarse layer. The filling ratio was 100% of the fine mesh porosity. All heat pipes were tested for five applied powers (10 W–50 W) in the horizontal orientation. A single heat pipe was also tested for multiple tilt angles (-90° to + 90°) and three condenser temperatures (30 °C–50 °C). A minimum thermal resistance in the horizontal orientation of 0.107 K/W was observed for 50 W and the 1.58 mm thick heat pipe. This design had the smallest wick mesh (#200) and the largest coarse support mesh (#12).

Chen et al. [92] designed a thin copper heat pipe (104 mm × 14 mm × 0.4 mm) using wet etching and diffusion bonding, with water as the working fluid (see Fig. 11). The wicking structure was a woven copper mesh (#300), while wet etched copper micropillars of varying diameters (100 μm and 70 μm) were used for structural support (150 μm thick). The heat pipe was tested for varied applied power (2 W–6 W), in multiple orientations, for a filling ratio of 120% of the mesh void volume. In the horizontal orientation, the heat pipe dissipated 4.5 W for a thermal resistance of 1.06 K/W and achieved a minimum thermal resistance of 0.6 K/W for an applied power of 2 W.

Table 4 provides a summary of the research covered in Section 2.2. A similar methodology as Table 3 was applied when collating the data. The most common keywords for these works are thermal resistance (× 6), thermal performance (× 6), electronic cooling (× 4), ultra-thin heat pipe (× 3), ultra-thin flattened heat pipe (× 3), heat pipe (× 3), and filling ratio (× 3).

In the contexts of flexible heat pipe technology for foldable electronic devices, optimisation of the internal vapour core thickness [2,5,70,87] and working fluid selection [68] are integral design components for ultra-thin flexible heat pipe technology. Similar to Section 2.1, the application of composite wicking structures [67,71,72,74,75,77,87] and surface wettability augmentation [86] will maximise the flexible heat pipe performance given the package size limitation of foldable electronic devices. The implementation of shell materials such as silicon [110], liquid-crystal polymer films [79], and polyimide [78] are important steps towards the flexible shell materials required to enable foldable heat pipe technology.

2.3. Macro flexible heat pipes

Non-flexible heat pipes are not compatible with the cooling of compact, foldable electronic devices or applications where there is large-scale relative movement between heat sources and heat sinks [64–66]. Bendable or flexible heat pipes [64,81–83] have attracted significant attention. They can allow for deformation while maintaining their excellent heat-transfer performance and provide device designers with more freedom than current rigid heat transfer systems [81].

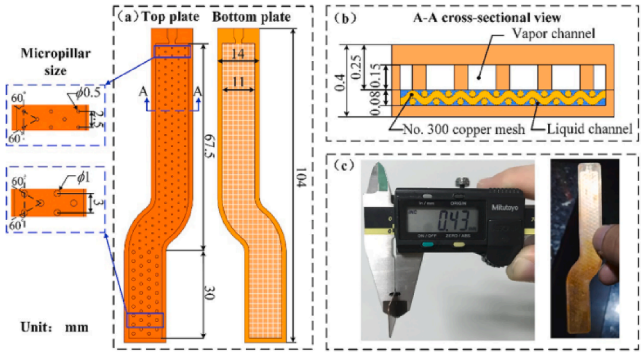

Fig. 11. Schematic diagrams of the heat pipe: (a) top-view schematics of the top and bottom plates, (b) cross-sectional schematic of the heat pipe, and (c) photographs of the heat pipe [92].

2.3.1. Cylindrical, flexible heat pipe

Yang et al. [64] constructed a flexible tube heat pipe using water as the working fluid (Fig. 12). The heat pipe integrated a flexible polyurethane polymer connector (OD = 8 mm, ID = 5 mm, and L = 100 mm) between the rigid copper condenser (OD = 5 mm, ID = 4 mm and L = 150 mm) and evaporator (OD = 5 mm, ID = 4 mm and L = 150 mm). The copper and the polyurethane tubes were bonded together using an adhesive (Tianshan Mountains, Beijing, Adhesive TS1415) at room temperature for 24 h. A tightening belt further mechanically strengthened the bonding. The wick consisted of a 320 count superhydrophilic (strong-base-oxidized) copper woven mesh. The heat pipe was characterized for three filling ratios (20%–40%), five applied power levels (2 W–12 W), and five bend angles (0°–120°). It was tested exclusively in the vertical orientation with the condenser directly above the evaporator when the bend angle was zero. A minimum thermal resistance of 0.008 K/W was reported for the 30% filling ratio case at the maximum bend angle and applied power of 12 W.

Yang et al. [81] constructed a flexible heat pipe using a fluororubber tube (OD = 8 mm, ID = 5 mm, and L = 150 mm) as a flexible midsection and copper tube for the evaporator (OD = 5 mm, ID = 4 mm, and L = 150) and condenser (OD = 5 mm, ID = 4 mm, and L = 150) sections (Fig. 13). A strong base treated hydrophilic layered copper mesh was incorporated as the wick structure, and deionized water was chosen as working fluid. The treated copper meshes were wrapped onto a stainless-steel spring with an outer diameter of 3 mm and a wire diameter of 0.3 mm. The spring ensured conformal deformation of the rubber tube and good contact between copper mesh wick and rubber tube inner surface during bending. The heat pipe was characterized for three filling ratios (10%–30%), six power levels (2 W–12 W), and five bend angles (0°–180°). The heat pipe was tested in the horizontal orientation; the condenser and evaporator remained on the same plane for all bend angles, limiting the impact of gravity on fluid-vapour circulation. At the 180° bend angle and a 20% filling ratio, a minimum thermal resistance of ≈0.62 K/W was achieved for a 12 W power input [81].

Jaipurkar et al. [82] explored two flexible copper heat pipes of varied diameter (ID = 6 & 10 mm and 270 mm long) with a stainless steel bellow to enable articulation (Fig. 14). The heat pipes had a woven screen mesh made of phosphor bronze for the wick, and deionized water was used as the working fluid. The heat pipes were characterized for a range of applied power inputs (10 W–110 W), two bend angles (0° and 10°), and an unspecified optimized filling ratio. The authors noted that the water collected in the grooves of the bellows during testing. The heat pipe was tested in the vertical and horizontal orientation for both cases. In the vertical orientation with no bend angle, the condenser was directly above the evaporator. No information on the condenser and evaporator relationship was noted in the horizontal bent condition. For the 6 mm heat pipe, dry-out occurs earlier in horizontal operation than the 10 mm counterpart (60 W vs 90 W). The flexed heat pipe was noted to outperform its straight counterpart for all orientations and sizes except the 10 mm ID, vertical condition. The authors suggested this was due to the improved thermal contact between the wick and inner walls of the evaporator and condenser. At the 10° bend angle, in the horizontal orientation, a thermal resistance of ≈0.27 K/W was achieved for a 50 W power input [82].

Huang et al. [83] developed a multistage flexible heat pipe inspired by the structure of the human spine (see Fig. 15). Their design consisted of several stiff copper tubes and a continuous flexible polymer shell (heat-shrinkable sleeve). Two layers of polyvinyl chloride (PVC) sealing tapes were used between the copper tube and the heat-shrinkable sleeve for sealing. The copper tubes were first twined by the PVC sealing tape. Then, the gap was filled with an adhesive (TS 1415). The resulting tube was then wrapped with the heat-shrinkable sleeve and heated by a heat gun to increase the shell's strength. After heating, the heat-shrinkable sleeve shrank and tightly bonded with the tube. A hydrophilic copper mesh was then tightly inserted into the tube to serve as a wick structure,

Table 4
Ultra-thin heat pipe summary.

Ref	Year	Type	Base material	Dimension	Internal chamber height	Wick	Working fluid	Orientation	Gravity assisted	Cooling medium	Operating temperature range [°C]	Power [W]	Thermal resistance [K/W]	Thermal conductivity [W/m K]
Aoki et al. [86]	2010	Flat, flattened	Copper	150 mm × 9 mm × 1 mm (L × W × H)	N/A	copper mesh (#100)	water	horizontal	No	Water, forced convection	45–53	20	0.20	4.5×10^4
Aoki et al. [86]	2010	Flat, flattened	Copper	100 mm × 9 mm × 0.7 mm (L × W × H)	N/A	copper mesh (#100)	water	horizontal	No	Water, forced convection	48–52	7	0.40	3.3×10^4
Li et al. [67]	2016	Flat, flattened	Copper	200 mm × 7.8 mm × 1 mm (L × W × H)	N/A	copper sintered powder	water	horizontal	No	Water, forced convection	53–59	12	0.29	6.7×10^3
Yang et al. [71]	2017	Flat, flattened	Copper	100 mm × 9.1 mm × 1 mm (L × W × H)	N/A	copper braided composite wire	water	horizontal	No	Water, forced convection	NA	20	0.12	5.2×10^4
Zhou et al. [75]	2017	Flat, flattened	Copper	100 mm × 2.7 mm × 0.8 mm (L × W × H)	N/A	copper foam (80% porosity)	N/A	horizontal	No	Water, forced convection	50–55	5	0.74	4.3×10^3
Zhou et al. [72]	2019	Flat, flattened	Copper	100 mm × 7.7 mm × 1.1 mm (L × W × H)	N/A	copper monoporous spiral woven mesh	water	horizontal	No	Water, forced convection	70–75	26	0.09	10.6×10^4
Zhou et al. [72]	2019	Flat, flattened	Copper	100 mm × 7.7 mm × 1.1 mm (L × W × H)	N/A	copper biporous spiral woven mesh	water	horizontal	No	Water, forced convection	69–73	24	0.10	9.6×10^4
Zhou et al. [72]	2019	Flat, flattened	Copper	100 mm × 7.7 mm × 1.1 mm (L × W × H)	N/A	copper biporous spiral woven mesh	water	horizontal	No	Water, forced convection	65–69	18	0.14	7.2 s × 10^4
Zhou et al. [87]	2019	Flat, flattened	Copper	120 mm × 9 mm × 0.75 mm (L × W × H)	0.35 mm	copper mesh (#100)	water	horizontal	No	Water, forced convection	61–65	8.50	0.28	4.2×10^4
Zhang et al. [80]	2019	Flat, flattened	Aluminium	200 mm × 26 mm × 1.5 mm (L × W × H)	N/A	aluminium fibre	Acetone	Inclined 30°	Yes	Water, forced convection	25–29	25	0.13	3.2×10^4
Ivanova et al. [110]	2006	Flat	Silicon	50 mm × 50 mm × 1 mm (L × W × H)	N/A	silicon micro capillary wick	water	horizontal	No	Water, forced convection	50–120	75	0.90	521
Ding et al. [93]	2010	Flat	Titanium	30 mm × 30 mm × 0.6 mm (L × W × H)	N/A	titanium pillars	water	horizontal	No	Liquid nitrogen, N/A	85–105	7.20	2.69	350
Oshman et al. [79]	2011	Flat	Liquid crystal polymer, copper, glass	60 mm × 30 mm × N/A mm (L × W × H)	N/A	copper mesh (#200)	water	horizontal	No	Water, forced convection	43–58	11.94	1.11	695
Lewis et al. [78]	2015	Flat	Polyimide, SU-8, TiO2	60 mm × 20 mm × 0.3 mm (L × W × H)	N/A	SU-8 pillars	water	horizontal	No	Coolant, forced convection	25–98	9.54	11.92	594
Yang et al. [111]	2015	Flat	FR4, copper	35 mm × 40 mm × 2 mm (L × W × H)	N/A	copper mesh (#200)	water	horizontal	No	Water, forced convection	25–94	18	3.84	N/A
Li et al. [74]	2016	Flat	Copper	100 mm × 50 mm × 2 mm (L × W × H)	N/A	copper powder	Water	horizontal	No	Water, forced convection	36–65	120	0.20	2.8×10^3
Lv et al. [77]	2017	Flat	Copper	100 mm × 50 mm × 0.95 mm (L × W × H)	N/A	copper mesh (#150)	water	horizontal	No	Water, forced convection	38–51	30.25	0.39	3.7×10^3

(*continued on next page*)

Table 4 (*continued*)

Ref	Year	Type	Base material	Dimension	Internal chamber height	Wick	Working fluid	Orientation	Gravity assisted	Cooling medium	Operating temperature range [°C]	Power [W]	Thermal resistance [K/W]	Thermal conductivity [W/m K]
Chen et al. [73]	2019	Flat, stamping	Aluminium	120 mm × 120 mm × 2 mm (L × W × H)	N/A	aluminium triangular microgrooves	Acetone	horizontal	No	Water, forced convection	31–57	160	0.16	N/A
Huang et al. [91]	2019	Flat	Copper	100 mm × 65 mm × 1.5 mm (L × W × H)	N/A	copper mesh (#100 / 200)	water	horizontal	No	Water, forced convection	62–74	50	0.20	2.8×10^3
Chen et al. [92]	2019	Flat	Copper	104 mm × 14 mm × 0.4 mm (L × W × H)	0.23 mm	copper mesh (#300)	Water	horizontal	No	Water, forced convection	51–56	4.50	1.06	1.4×10^4
Li et al. [112]	2019	Flat	Copper	100 mm × 50 mm × 0.5 mm (L × W × H)	0.3 mm	copper mesh (#150)	Water	horizontal	No	Air, natural convection	72.3–72.5	7.37	0.09	2.9× 104

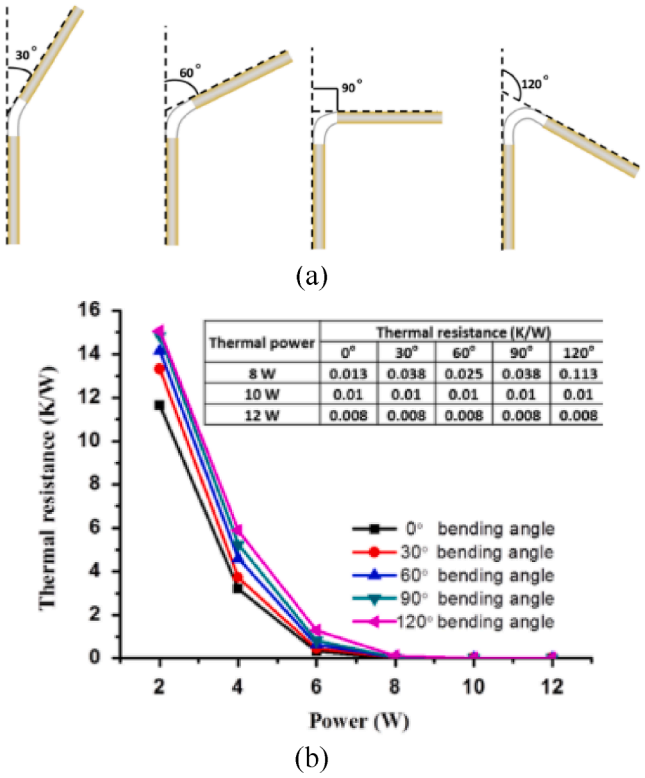

Fig. 12. (a) Thermal resistance of flexible heat pipes filled with 30% working fluid bent at different angles, and (b) schematic illustration of bending experiments [64].

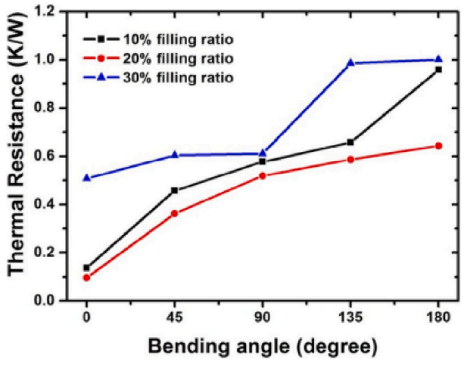

Fig. 13. Thermal resistance variation of flexed heat pipes with three different filling ratios (10%, 20%, and 30%) under a heating power input of 12 W [81].

and deionized water was used as the working fluid. The #300 copper mesh was hydrophilically treated using a mixed solution of $K_2S_2O_8$ (0.065 mol/L) and KOH (2.5 mol/L). The overall length of the flexible heat pipe was 220 mm; the outer/inner diameters were 6/5 mm. Four copper tubes of length 15 mm were arrayed in the adiabatic section. The length of the two ends of the copper tubes was 75 mm, while a 2 mm spacing was maintained between connecting tubes. The two layers of copper mesh were 210 mm long. The heat pipe was tested for four filling ratios (15% – 45%), five applied power levels (6 W – 14 W), and five bend angles (0° -‘ 180°). Huang et al. characterized their device in the horizontal and vertical direction, with and without gravity, using their articulating testbed. For the horizontal orientation, at a 180° bend angle, with no gravity assistance and a 25% filling ratio, a thermal resistance of ≈0.81 K/W was noted for a 10 W power input [83].

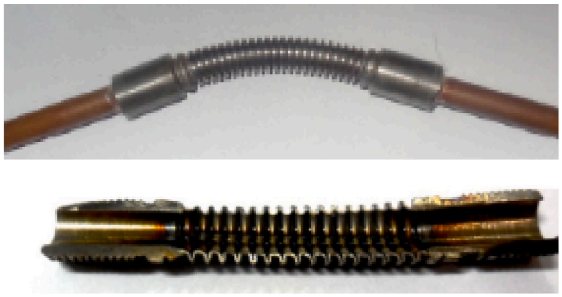

(a)

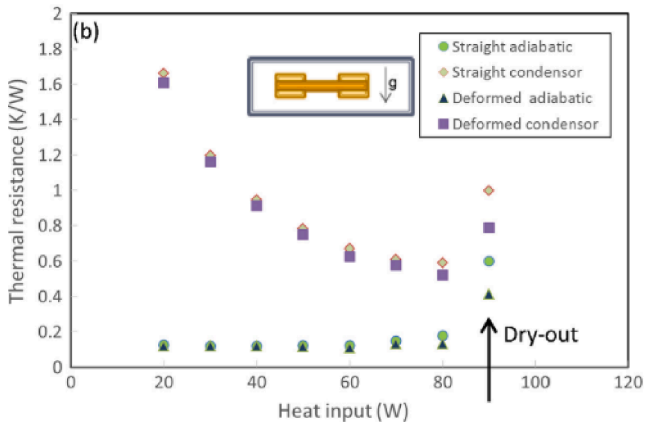

(b)

Fig. 14. (a) Prototype flexible heat pipe with bellow section and copper, and (b) thermal resistance 10 mm ID heat pipe in both straight and deformed configurations for the heat pipe's horizontal position [82].

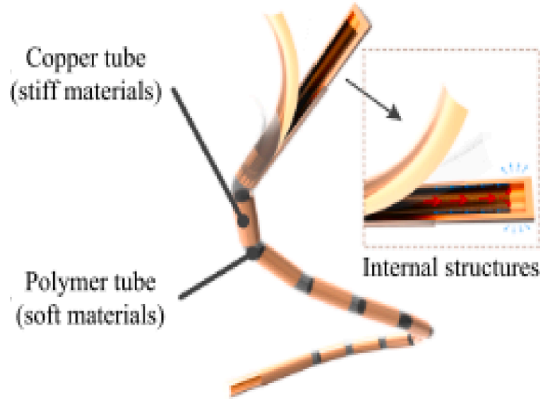

Fig. 15. Multistage flexible heat pipe inspired by the structure of the human spine [83].

2.3.2. Flat plate flexible heat pipe

Hsieh and Yang [84] investigated a polymer-based flexible flat heat pipe (FHP) for 0°– 90° bending angle (Fig. 16). The heat pipe was 80 mm × 20 mm × 4 mm in size. Silicone rubber was used as a shell material with copper-filled thermal vias were embedded in the evaporator and condenser sections to increase the thermal conduction through the casing wall. Two layers of #250 copper mesh were used as the wicking material on the top and bottom of the internal chamber, and deionized water was implemented for the working fluid. A mesh-type copper pillar was positioned along the centerline of the internal cavity. The heat pipe was tested for four filling ratios (25%–50%), thirteen applied power levels (1 W–12.7 W), and six bend angles (0°–90°). A minimum thermal resistance of 5.93 K/W was observed for a bending angle of 15°, at a 40% filling ratio and an applied power of 12.67 W, where the condenser was angled above the evaporator. Larger bend angles resulted in a decrease in the thermal resistance of the heat pipe.

A summary of the key heat pipe characteristics is shown in Table 5. A similar methodology as Table 3 and 4 was applied when collating the data. The maximum bend angles were picked as they are the most pertinent factor to the present review. The most common keywords for these works are flexible heat pipe (× 4), thermal resistance (× 3), and thermal performance (× 2).

2.4. Ultra-thin flexible heat pipes

Wu et al. [94] developed a heat pipe (110 mm × 20 mm × 1.8 mm) fabricated from polyethylene-terephthalate, copper mesh, copper tape, and rubber (see Fig. 17). The heat pipe was sealed using hot lamination and used methanol as the working fluid. It was characterized in the horizontal orientation for a varied applied power (5 W–40 W), filling ratio (18.6%, 36.9%, and 66.4%), and bend angle (0°, 30°, and 45°). The authors noted delamination of the polyethylene-terephthalate for applied powers > 30 W and filling ratios > 18.6% due to increased methanol vapour pressure. A thermal resistance of 0.16 K/W and ≈1.14 K/W was noted for applied power of 26 W and 35 W for a bend angle of 0° and 45°, respectively [94].

Oshman et al. [95] constructed a thin, flexible flat plate heat pipe (130 mm × 70 mm × 1.31 mm) with water as the working fluid. A commercially available low-cost film composed of laminated sheets of low-density polyethylene terephthalate, aluminium, and polyethylene layers (Mylar) were used as the casing. A triple-layer sintered 200 count copper mesh (51 μm wire diameter, 76 μm spacing) served as a wicking structure. After sintering, the meshes were coated with an atomic layer deposited Al2O3/SiO2 bi-layer coating, promoting nucleation, adhesion, and wettability of the mesh with water. A coarse nylon woven mesh (0.438 mm wire diameter, 0.823 mm spacing) provided space for vapour transport and mechanical rigidity. The heat pipe was sealed using thermal bonding. Testing investigated a thermal transport of 3.5 W–21.6 W, while the device was flexed at 0°, 45°, and 90°, with the evaporator maintained above the horizontal condenser. The heat pipe transported the maximum thermal power of 21.6 W for a thermal resistance of ≈1.35 K/W, ≈1.8 K/W, and ≈2.4 K/W for the 0°, 45°, and 90° bend angles, respectively. A minimum thermal resistance for the 90° bend angle occurred at ≈14.4 W of 1.28 K/W [95].

Lee and Byon [96] fabricated a flexible, thin flat plate copper heat pipe (106 mm × 36 mm × 1 mm) with water as the working fluid (see Fig. 18). The wicking structure consisted of a single layer of chemically oxidized 200 count copper mesh (51 μm wire diameter, 76 μm spacing). Three coarse mesh layers were stacked on top to provide structural support and vapour passage. All layers are bonded via spark plasma sintering. The heat pipe was tested for varied applied power (0.19 W–5.5 W) and two bending angles (0° and 64°(95 mm radius of curvature)) in the horizontal orientation. An optimum effective thermal conductivity of ≈1160 W/(m K) was observed for the flexed heat pipe at an applied power of ≈0.19 W. A further increase in the applied power results in a decrease in the heat pipe effective thermal conductivity, with an effective thermal conductivity of ≈761 W/(m K) noted for an applied power of ≈5.4 W. The straight heat pipe had a higher effective thermal conductivity than its flexed counterpart for applied powers great than ≈1.33 W [96]. The authors noted that the reduced space of the vapour flow path yielded a significant pressure drop, reducing the performance of the flexed heat pipe.

Lim and Kim [3] fabricated a polymer-based flexible pulsating heat pipe (97.5 mm × 65.4 mm × 1 mm) with HFE-7000 as the working fluid. The heat pipe consisted of a multi-layer laminated film top and bottom layer (see Fig. 19) and a low-density polyethylene inner sheet, which was laser cut to 12 dual diameter channel of 1.4–0.7 mm. The heat-sealed flanges were covered with the indium coating to minimize the permeation of non-condensable gases in a lateral direction. Owing to the

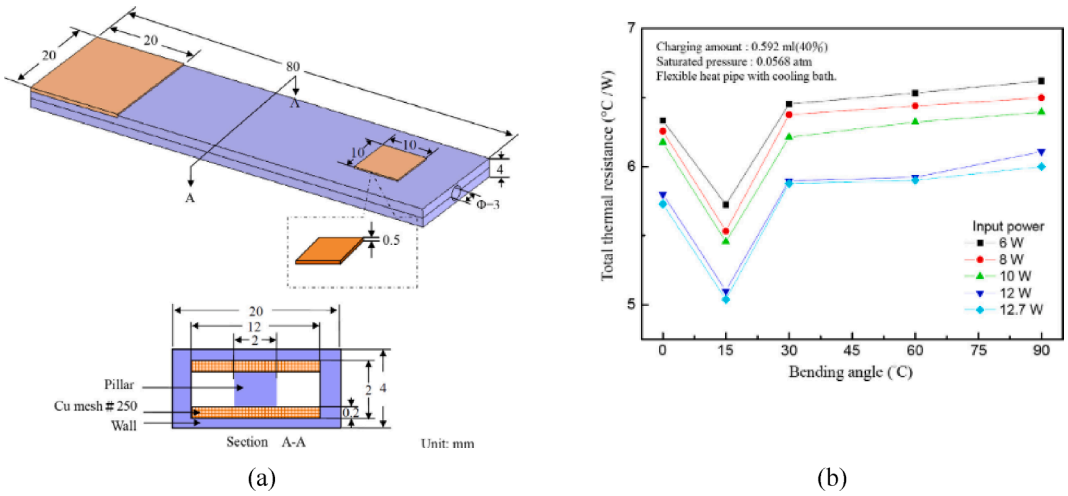

Fig. 16. (a) Schematic of the heat pipe used by Hsieh and Yang, and (b) total thermal resistance vs bending angle [84].

indium-coated flanges, the long-term reliability of the heat pipe drastically increased. The indium coating was covered with a flexible UV-curing resin (NOA68, Norland Products, Inc) to protect the metal coating from cracking under bending conditions. Testing consisted of varied applied power (2 W–16 W), four testing orientations, and a constant 50% filling ratio. The orientations investigated were vertical (condenser above evaporator), horizontal, vertical evaporator, and horizontal condenser with a 90° bend and horizontal evaporator and vertical condenser with a 90° bend. The heat pipe transported a maximum thermal power for a 90° bend with a vertical evaporator and horizontal condenser of 15 W with a thermal resistance of ≈2.53 K/W [3]. The maximum thermal transport and minimum thermal resistance in the horizontal condition occurred at 10 W and 6 W for a thermal resistance of 3.75 K/W and 3.3 K/W, respectively.

Liu et al. [97] investigated a flexible flat heat pipe (130 mm × 60 mm × 1.47 mm). They used an aluminium compound packing film for the casing, a three-layered gradient wetting stainless steel mesh (#200) covered with a nanowires wicking structure, and water as the working fluid (see Fig. 20). The casing material consists of layers of polyamide, aluminium, chlorinated-polypropylene, and bonding and insulating layers. It was sealed by hot pressing at 0.5 MPa and 155 °C. The three-layer wicking structure was embedded in chlorinated-polypropylene on the casing material's inner surface by hot pressing, reducing the contact thermal resistance, and tightly combining it to the surface during the bending process. The hydrophilic and hydrophobic properties of the wick were changed by the nanowire structure's surface catalytic growth. A polyethylene wire mesh (#20) was used as the support structure and to ensure vapour space during operation. The thermal resistance of the evaporator and condenser regions were minimized through laser ablation of the casing material. The heat pipe was tested for three heating powers (4 W–12 W), filling ratios (20%–40%), a range of bending angles (0°–180°), and condenser temperatures. The evaporator is maintained above the condenser when the heat pipe bend angle is >0°. The heat pipe transported the maximum thermal power of 12 W for a thermal resistance of 0.525 K/W and ≈2.25 K/W for the 0° and 180° bend angles, respectively [97]. Liu et al. attributed the increase in thermal resistance for increasing bend angle to obstruction of the vapour transport process in the adiabatic section, which leads to increased liquid-vapour interfacial thermal resistance in the evaporation section.

Jung et al. [90] developed a flexible polycarbonate core pulsating heat pipe (130 mm × 60 mm × 0.64 mm) that is hermetically sealed using a polyimide and copper casing (70 μm thick). The pulsating heat pipe consisted of 15 turns with dual-diameter channels (channel width 1 = 1.5 mm, channel width 2 = 0.5 mm, and channel height 0.5 mm) and used HFE-7000 as the working fluid. The heat pipe was tested in three orientations (horizontal, vertical, and vertical 45° bend). The condenser was maintained above the evaporator in the vertical and vertical 45° bend conditions for a range of applied thermal powers (3 W–26 W). The heat pipe transported a maximum thermal power of 18 W, 26 W, and 24 W for effective thermal conductivities of ≈792 W/(m K), 1070 W/(m K), and ≈1032 W/(m K) for the horizontal, vertical and vertical 45° bend orientations, respectively [90].

Nematollahisarvestani et al. [113] numerically compared the thermal management performance of a graphite heat spreader, two vapour chambers with a graphite hinge, and a single, large, and foldable vapour chamber for a foldable mobile electronic device (144 × 138.3 mm^2). Two heat sources representing the main processor (14.45 × 14.41 mm^2, 3.3 W) and a broadband processor (8.26 × 9.02 mm^2, 2.5 W) were implemented. The modelled graphite sheet was 144 × 138.3 mm^2 (L × W), and a thickness of 400 μm with a through-thickness thermal conductivity of 2.8 W/(m K), and the in-plane thermal conductivity of 500 W/(m K). For the second case, with two vapour chambers connected by a graphite bridge, The bridge is 138.3 × 20 mm^2, a thickness of 300 μm and a through-thickness thermal conductivity equal to 3.5 W/(m K), and the in-plane thermal conductivity of 600 W/(m K). The modelled vapour chambers' total thickness was 385 μm, with a 160 μm thick vapour core and 75 μm thick walls and wick. The authors explored several hinge geometries for the final case of a foldable vapour chamber; these included straight, wavy, torsional, and arrays of inclined torsional joints and bridges. Using a graphite heat spreader in the fully unfolded configuration, a temperature difference of 17 °C was calculated across the device. For the design using two vapour chambers connected by a graphite bridge, the temperature difference was 7.2 °C. Finally, for the design using a single large foldable vapour chamber, the temperature difference is only 1–2 °C.

Table 6 provides a summary of the research covered in Section 2.4. A similar methodology, as outlined previously, is applied when collating the data. The most common keywords for the research covered in this section are flexible heat spreader (× 2), long-term reliability (× 2), and pulsating heat pipe (× 2).

2.5. Summary

Fig. 21 synthesizes the data from Sections 2.1–2.4 and Tables 3–6 to compare the reported heat pipe thermal characteristics. The filled markers denote when the entire top surface is implemented as a condenser. In this configuration, heat is typically applied centrally, and heat transfer paths are facilitated laterally and vertically through the heat pipe. Whereas for the empty markers, there exists an adiabatic section where heat is transported in one direction along the heat pipe.

Table 5
Flexible macro heat pipe summary.

Ref	Year	Type	Base material	Flexible material	Dimension	Wick	Working fluid	Orientation	Gravity assisted	Cooling medium	Operating temperature range [°C]	Bend Angle [°]	Power [W]	Thermal resistance [K/W]	Thermal conductivity [W/m K]
Yang et al. [64]	2015	tube flexible	copper	polyurethane tube	8 mm × 400 mm (OD × L)	copper mesh (#300)	Water	Vertical	Yes	Water, forced convection	15	120	12	0.01	≈7.6× 10^5
Yang et al. [81]	2016	tube flexible	copper	fluororubber tube	8 mm × 450 mm (OD × L)	copper mesh (#300)	Water	Horizontal	No	Water, forced convection	10–56	180	12	≈0.62	≈1.2 × 10^4
Jaipurkar et al. [82]	2017	tube flexible	copper	stainless steel bellows	9.8 mm × 270 mm (OD × L)	phosphor bronze mesh	Water	Horizontal	N/A	Water, forced convection	25–39	10	50	≈0.27	≈2.2 × 10^4
Huang et al. [83]	2020	tube flexible	copper	polymer heat-shrinkable sleeve	6 mm × 220 mm (OD × L)	copper mesh (#300)	Water	Horizontal	Yes	Air, forced convection	N/A	180	10	≈0.81	≈5.6× 10^3
Hsieh and Yang [84]	2013	flat, flexible	Silicone rubber	Silicone rubber	80 mm × 20 mm × 4 mm (L × W × T)	copper mesh (#250)	Water	Horizontal	Yes	Water, forced convection	25–100	90	12.7	≈5.93	≈84

Fig. 21a contrasts the applied thermal power transferred by the heat pipe and heat pipe thermal resistance. Generally, it can be seen that the macro-scale rigid and rigid ultra-thin heat pipes transfer larger thermal powers for lower thermal resistances (temperature drop between evaporator and condenser). In contrast, the flexible macro-scale and ultra-thin heat pipes transfer lower thermal powers for higher thermal resistance. Fig. 21b contrasts the applied power with the heat pipe thermal conductivity. The ultra-thin rigid heat pipes are noted to have the greatest thermal conductivities. The macro-scale rigid heat pipes show low thermal conductivities but the largest thermal power transferred. Both flexible cases, macro-scale and ultra-thin, demonstrate intermediate thermal power transfer and thermal conductivities. The flexible heat pipes' lower thermal performance is sensible, given the performance penalties highlighted by numerous studies in Sections 2.1 and 2.4. The most prominent are (i) the altered vapour space and wicking structure when the heat pipe is deformed, limiting working fluid recirculation. (ii) the typically lower thermal conductivity of the flexible materials employed in the heat pipe casing, and (iii) the difficulty in maintaining high-vacuum due to these more permeable casing materials than their rigid counterparts. Fig. 21 highlights the promising work completed in the field of flexible heat pipes and demonstrates the work yet to be completed. This work is discussed in Section 3.

3. Open research questions, challenges, and potential solutions

From the discussed literature, it is clear that ultra-thin heat pipe technology is still a largely underdeveloped topic. Given the discussed state-of-the-art and incorporating suggestions from previous review articles [1,62], the following are potentially impactful topics for future research in the field of ultra-thin flexible heat pipes. At normal operating temperature, the heat transfer performance of a heat pipe is limited by the wick capillary pressure. The pressure balance inside a heat pipe at equilibrium is given by [92]:

$$\Delta P_{cap} \geq \Delta P_v + \Delta P_l + \Delta P_g \tag{1}$$

where ΔP_{cap} is the capillary force provided by the wick, ΔP_v is the vapour pressure from the evaporation section to the condensation section, ΔP_l is the liquid pressure drop from the condensation section to the evaporation section, and ΔP_g is the pressure drop due to gravity.

3.1. Shell material

The starting point in the development of flexible, ultra-thin heat pipes is investigating a suitable shell material. Potentially promising materials are polymer-based casings. The significant advantages of using polymers in the development of an ultra-thin flat plate heat pipe are their lightweight, flexibility, chemical resistance, electrical insulating characteristics, and compatibility with most electronics fabrications [84,111]. The literature has highlighted some challenges to the adoption of polymer heat pipes.

1. Polymers generally possess lower thermal conductivities than metals. This can be overcome using thermal vias [79,84,111].
2. Metal wick structures, such as sintered copper powder and meshes, cannot be sintered together with the polymer casing, increasing their thermal resistance [1,97].
3. Polymer-based heat pipes can yield outgassing problems, as well as the generation of non-condensable gases limiting long-term reliability. Solutions include incorporating a flexible gas barrier, such as aluminium foil [3], or a coating such as indium [3] or copper [79].
4. Polymers generally have lower wettability with working fluids [96]. This may be advantageous for promoting drop-wise condensation in the condenser section. This can be overcome by utilizing a sufficiently hydrophilic wicking structure or augmented evaporator section [106].

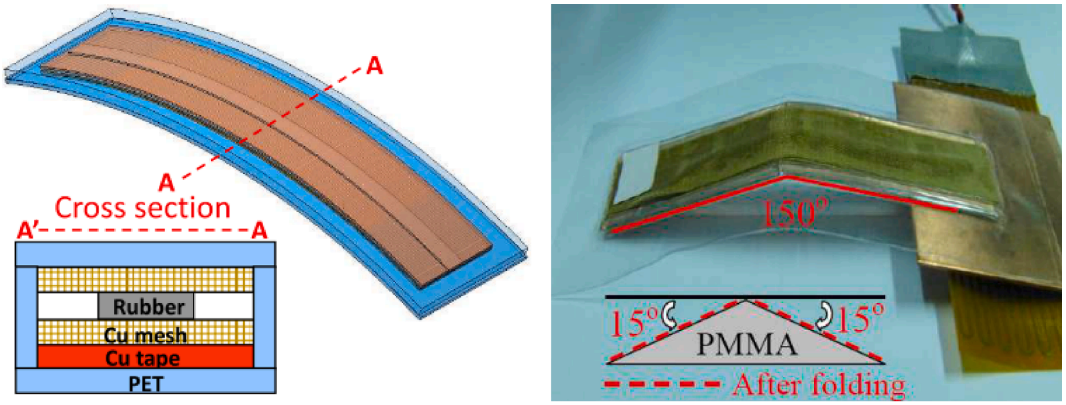

(a) (b)

Fig. 17. (a) Structure of the flexible heat pipe, and (b) thermal resistance test at 30° bending angle [94].

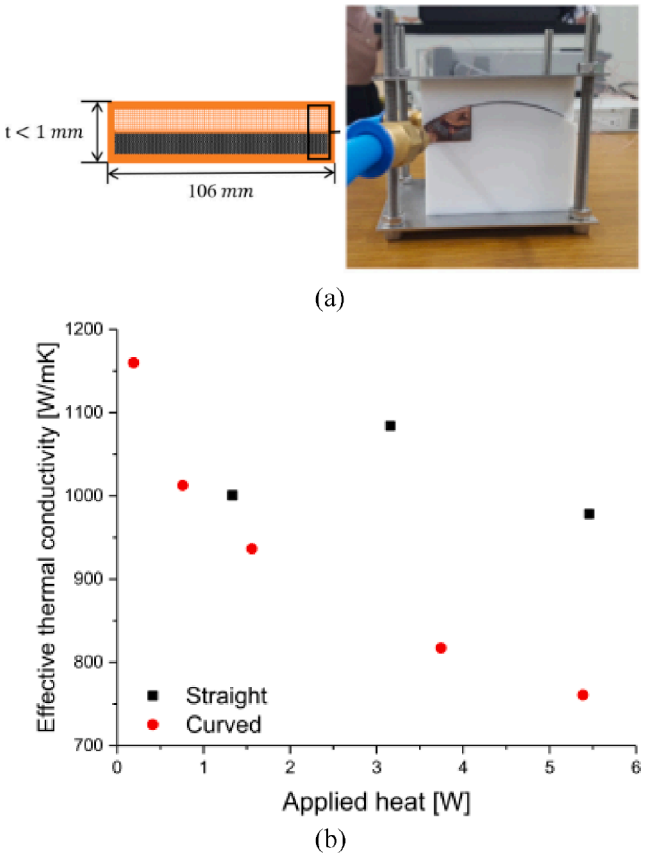

Fig. 18. (a) Heat pipe structure and testing bend, and (b) comparison of the thermal performances of curved and straight flexible heat pipes [96].

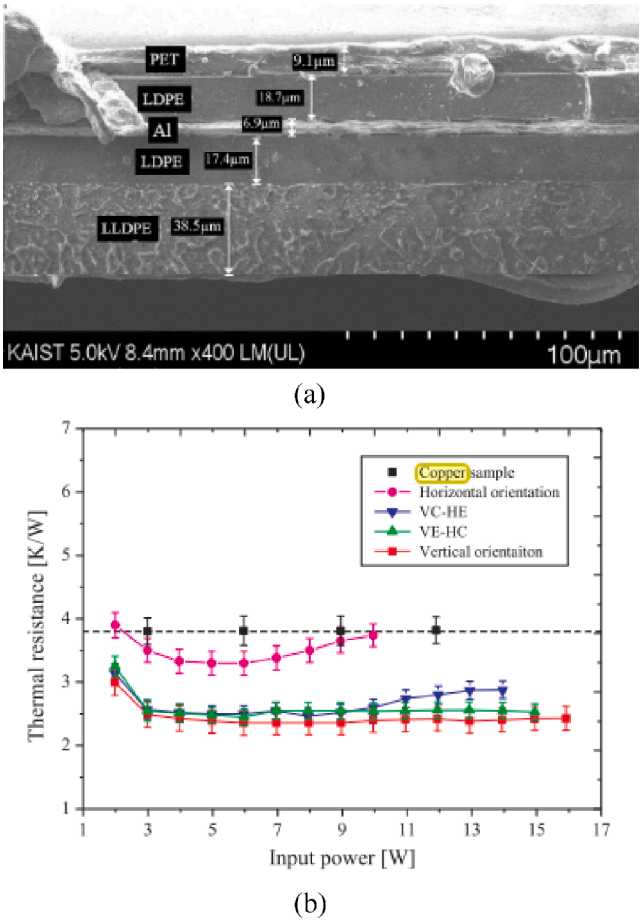

Fig. 19. (a) SEM image of the multilayer laminated film, and (b) thermal resistances of the copper reference sample and FPHP for varied input powers [3].

Polyimide [78], ultra-thin copper [92], and hybrid materials incorporating non-permeable layers [95,97] provide promising flexible casing materials. Integration and joining the flexible material to a rigid section (with higher wall conductivity) are also worth considering. Challenges here include maintaining minimal thickness while not sacrificing internal vapour core thickness. Close integration with material sciences will be crucial to the development of a future solution.

An evident challenge for flexible heat pipe technology is the disruption of normal vapour flow and fluid recirculation during articulation, which leads to increased liquid-vapour interfacial thermal resistance in the evaporator section [81]. Articulation can lead to the formation of a liquid plug in the internal cavity [83] due to the reduced effective channel area of the wick for fluid flow as the heat pipe curvature increases, resulting in a reduced allowable heat dissipation rate [96]. This can be reduced by implementing a support structure at the articulation joint to prevent vapour space collapse. In tandem, the heat pipe can incorporate design for articulation (a bend line), reduced performance while folded, and then normal performance when open. Full performance might only be needed when the foldable device is open.

Liu et al. [97] defined the additional hydraulic pressure loss for their ultra-thin flat heat pipe when the vapour goes through the bending section:

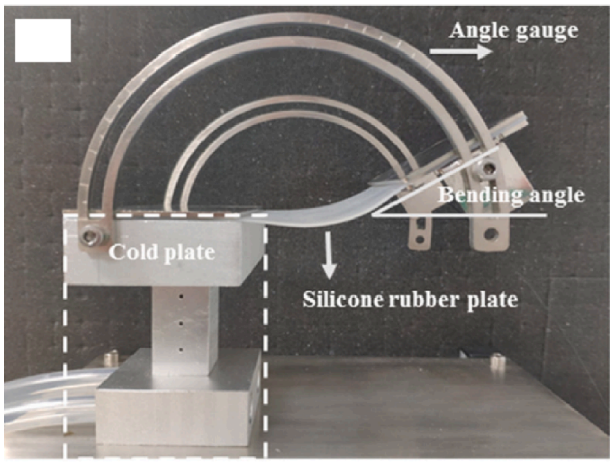

(a)

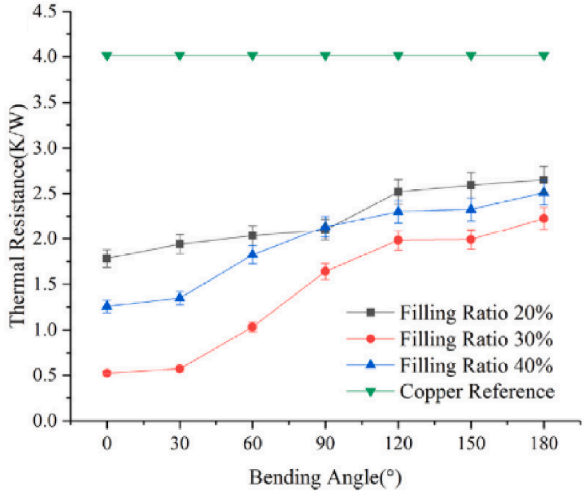

(b)

Fig. 20. (a) Multi-angle heat transfer platform, and (b) thermal resistance of the flexible flat heat pipe for 35 °C condensation temperature and 12 W applied power [97].

$$\Delta P_{bend} = \varsigma \frac{v^2}{2g} \tag{2}$$

$$\varsigma = \left[0.131 + 0.159\left(\frac{L_{char}}{r_c}\right)^{3.5}\right]\frac{\phi_{bend}}{90}$$

where v is the vapour velocity, L_{char} is the characteristic length in the direction of the thickness of the heat pipe, ϕ_{bend} is the bending angle and r_c is the radius of curvature in the adiabatic section. From the above relationship, it can be seen that as the bending angle increases, the hydraulic loss increases. Eq. (2) can be incorporated into Eq. (1) to give an updated pressure balance for a flexible heat pipe:

$$\Delta P_{cap} \geq \Delta P_v + \Delta P_l + \Delta P_g + \Delta P_{bend} \tag{3}$$

3.2. Porous wick structure

As seen in Eq. (3), the capillary wick inside a heat pipe should be able to provide sufficient capillary force as well as space for vapour flow, which is required to achieve the desired heat transfer performance. According to the Young-Laplace formula, ΔP_{cap} can be calculated by [77,92,114]:

$$P_{cap} = \frac{2\sigma\cos\theta}{r_{eff}} = \frac{2\sigma}{r_{cap}} \tag{4}$$

where σ is the surface tension of the working fluid, θ is the working fluid-wick contact angle, r_{eff} is the effective capillary radius of the wick and r_{cap} is the capillary radius. For a mesh screen, the effective capillary radius is equal to the distance between the wires in the mesh ($r_{eff} = \frac{w+d_w}{2}$) [92,96], where w is the spacing between wires and d_w is the wire diameter. While for channels between micropillars, the capillary radius is equal to half the channel width [78]. The employed wick should maximize hydrophilicity and permeability; some strategies include:

1. Surface oxidation [64,71,86,96], chemical corrosion [80] and deposition to form a micro-/nano-structured morphology on the surface [79,93].
2. Maximizing the wicking potential using nanoscale wicks, such as carbon nanotubes [62].
3. Hybrid structures, such as grooves and fibres, and pillars/grooves and meshes/fibres [79,102,106]. Multi-scale wicks can meet the requirements for sufficient capillary force and low vapour flow resistance [77].
4. Spiral woven meshes consist of braided fibres enabling excellent flexibility, wicking potential, and it is well suited for manufacturing ultra-thin heat pipes [72].

The minimum possible wick thickness should be chosen such that the capillary pressure in the wick is twice the total pressure drop in the wick and the vapour core. The greater the wettability of the wick, the thinner it can be, maximizing the vapour space. Yang et al. [71] noted a 30–40% increase in their capillary pressure by reducing their wick-water contact angle from 54° and 0° through oxidisation of their composite braided wires wick.

K_l is the permeability of the wick. For the commonly applied screen mesh wick, this can be calculated using [77,115]:

$$K_l = \frac{d_w^2 \varepsilon^3}{122(1-\varepsilon)^2} \tag{5}$$

$$\varepsilon = 1 - \frac{1.05\pi N d_w}{4}$$

where N is the mesh number of the screen mesh, and ε is the porosity. For a grooved wick, the permeability is given by [116]:

$$K_l = \frac{d_h^2 \varepsilon}{2(fRe_{L,h})}$$

where d_h is the hydraulic diameter:

$$d_h = \frac{4A_l}{C_l}$$

where and C_l is the wetted perimeter of the liquid channel. For a monoporous structure, such as a sintered wick, the permeability can be defined by [117]:

$$K_l = \frac{d_p^2 \varepsilon}{32}$$

where d_p is the pore diameter. Table 7 lists the values of ΔP_{cap} and K_l given by the papers included in this review. The final two rows of the table are the calculated values for a 100 count ($w = 1.8 \times 10^{-4}$ m; d = 5.6×10^{-5} m) and 200 count ($w = 7.6 \times 10^{-5}$ m; d = 5.1×10^{-5} m) copper meshes using Eq. (4) and (5) assuming perfect wetting ($\theta = 0^{\circ}$) for comparison.

For hybrid or non-uniform wicking structure, a capillary rise characterization can be investigated similar to that conducted by Feng et al. [118] to determine the wick permeability and capillary pressure.

Table 6
Ultra-thin flexible heat pipe summary.

Ref	Year	Type	Base material	Dimension	Internal chamber height	Wick	Working fluid	Orientation	Gravity assisted	Cooling medium	Operating temperature range [°C]	Bend Angle [o]	Power [W]	Thermal resistance [K/W]	Thermal conductivity [W/m K]
Wu et al. [94]	2011	flat, flexible	PET	110 mm × 20 mm × 1.8 mm (L × W × H)	N/A	copper mesh	methanol	horizontal	no	Air, natural convection	40–80	45.00	35.00	1.14	1834
Oshman et al. [95]	2013	flat, flexible	LDPE, aluminium, polyethylene layers	130 mm × 70 mm × 1.31 mm (L × W × H)	0.7 mm	copper mesh (#200)	water	horizontal	no	Water, forced convection	10–28	90.00	14.38	1.28	554
Lee et al. [96]	2018	flat, flexible	copper	106 mm × 36 mm × 1 mm (L × W × H)	0.8 mm	copper mesh (#200)	water	horizontal	no	Water, forced convection	N/A	63.00	5.40	3.87	761
Lim et al. [3]	2018	flat, flexible, pulsating	LDPE, PET	97.5 mm × 65.4 mm × 1 mm (L × W × H)	0.81 mm	LDPE dual diameter channel (1.4 mm, 0.7 mm)	HFE-7000	vertical evaporator-horizontal condenser	yes	Water, forced convection	20–58	90.00	15.00	2.53	399
Liu et al. [97]	2019	flat, flexible	aluminium compound packing film	130 mm × 60 mm × 1.47 mm (L × W × H)	N/A	stainless steel three-layer mesh (#200)	water	evaporator above condenser	no	Water, forced convection	35–62	180.00	12.00	2.25	479
Jung et al. [90]	2020	flat, flexible, pulsating	polycarbonate	85.5 mm × 53.4 mm × 0.64 mm (L × W × H)	0.5 mm	polycarbonate dual diameter channel (1.5 mm, 0.5 mm)	HFE-7000	condenser above evaporator	yes	Water, forced convection	20–67	45.00	24.00	1.94	1032

Wick design for non-pulsating flexible heat pipes has been centred on a single [64,83,94,96] and multiple [82,95,97] monoporous meshes. Innovative multi-scale flexible wick structures similar to the rigid multi-scale wicks developed by Feng et al. [85] and Peng et al. [107] are yet to be realised. Challenges include facilitating a flexible wicking structure that enables a strong thermal connection to the shell material, high thermal conductivity, capillary pressure, and low permeability. Future solutions will incorporate a strong material science and surface wettability collaboration. Potential solutions include copper chemical-plating modified polyacrylonitrile-based carbon fibre wick [119], flexible graphene coated polyurethane [120], and laser-induced graphene on polyimide substrate [121], among others. Flexion of the porous structure and its subsequent impact on the wick capillary pressure and permeability is a topic yet to be investigated.

3.3. Vapour – fluid space design

The maximum heat transfer decreases with a decrease in the vapour chamber thickness [1]. The liquid and vapour spaces of the internal cavity require careful design optimization through numerical and analytical models. The study of flow boiling [122] and condensation [123] in ultra-confined spaces such as those found in ultra-thin heat pipes is an underdeveloped topic. Patankar et al. [5] suggested that the vapour – fluid space design should focus on optimising the vapour and wick domains.

1. The thermal resistance of vapour chambers becomes dominated by the temperature gradient in the vapour core as the thickness is reduced. An ultra-thin vapour core induces a high-pressure gradient, and hence a high saturation temperature gradient. Fluid thermophysical properties govern this thermal resistance. Such a high-temperature gradient along the vapour core leads to a high-temperature variation along the condenser surface [68].
2. Intelligent geometry configurations should be considered to minimize pressure drop (radial channels [109], leaf/blood capillary design [107]). This can be done through analytical and numerical modelling (multi-object genetic algorithms or topology optimization).

The design of the vapour-fluid space is intrinsically linked to the wick design and the outer shell layers' thickness. It is further discussed in the working fluid section below.

The heat and mass transfer in an ultra-thin heat pipe is realized by steam flow and condensate reflux [124]. The pressure drop due to the vapour flow (ΔP_v) can be calculated using the Hagen-Poiseuille equation [77,92]:

$$\Delta P_v = \frac{8\mu_v q_{max} L_{eff}}{\pi \rho_v A_v d_h^2 h_{fg}} \tag{6}$$

where μ_v is the dynamic viscosity of the vapour; q_{max} is the maximum power at the capillary limit; L_{eff} is the effective length for the heat pipe ($L_{eff} = \frac{L_e + L_c}{2} + L_a$). ρ_v is the vapour density; A_v is the cross-sectional area of the vapour channel; d_h is the hydraulic diameter of the wick ($d_h = \frac{2A_l}{C_l}$), where A_l is the cross-sectional area of the liquid channel and h_{fg} is the specific enthalpy of vaporization. Lee and Byon [96] defined the permeability of the vapour space (K_v) as:

$$K_v = \frac{t_v^2}{12}$$

where t_v is the thickness of the vapour space. ΔP_l can be calculated using Darcy's law [92,114]:

$$\Delta P_l = \frac{\mu_l L_{eff} q_{max}}{K \rho_l A_l h_{fg}} \tag{7}$$

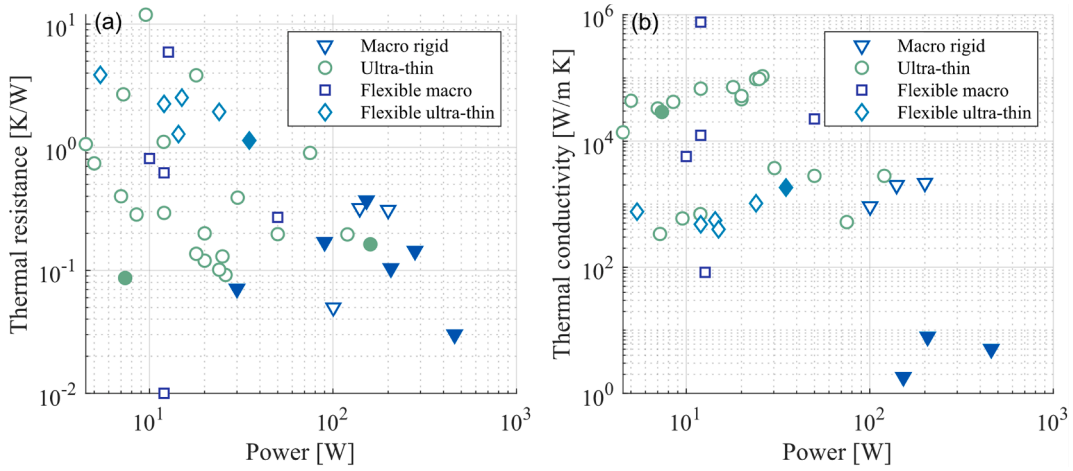

Fig. 21. Heat pipe data summary. Power compared with (a) thermal resistance and (b) thermal conductivity. Filled markers denote when the entire top surface is implemented as a condenser.

Table 7
Heat pipe wick performance comparison.

Ref	Wick	ΔP_{cap} [Pa]	r_{eff} [m]	K_l [m^2]
Feng et al. [85]	copper porous frustums and triangular channels, thermal spray	1013	–	3.37×10^{-11}
Aoki et al. [86]	copper mesh (#100)	–	1.2×10^{-4}	1.8×10^{-10}
Zhou et al. [87]	copper mesh (#100)	–	1.6×10^{-4}	–
Lv and Li [77]	copper mesh (#150)	1601	–	–
Peng et al. [107]	copper etched channels, leaf-vein-like fractal network	–	–	2.57×10^{-10}
Eqs. (4) and (5)	copper mesh (#100)	1160	1.2×10^{-4}	4.27×10^{-10}
Eqs. (4) and (5)	copper mesh (#200)	2135	6.4×10^{-5}	5.85×10^{-11}

where ρ_l is the density of the working fluid. According to Clausius-Clapeyron relation, the vapour pressure in the condenser section (P_{cond}) and the evaporator section (P_{evap}) can be calculated by [97,125]:

$$P_{cond} = P_\infty e^{\left(\frac{h_{fg}}{R_g}\frac{T_{cond}-T_\infty}{T_{cond}T_0}\right)} \tag{8}$$

$$P_{evap} = P_\infty e^{\left(\frac{h_{fg}}{R_g}\frac{T_{evap}-T_{cond}}{T_{evap}T_{cond}}\right)} \tag{9}$$

where P_∞ and T_∞ is the ambient pressure and temperature, respectively and R_g is the gas constant. The pressure drop due to gravity is given by:

$$\Delta P_g = \rho_l g L_{eff} sin\phi_{incl} \tag{10}$$

where g is the acceleration due to gravity, ϕ_{incl} is the inclination angle of the heat pipe. Combining the above equations, assuming a horizontal heat-pipe orientation, the maximum power at the capillary limit is given by [92]:

$$q_{max} = \frac{2\sigma\cos\theta}{r_{eff}L_{eff}}\left[\frac{8\mu_v}{\rho_v A_v r_h^2 h_{fg}} + \frac{\mu_l}{K_l \rho_l A_l h_{fg}}\right]^{-1} \tag{11}$$

Chen et al. [92] showed close agreement between their calculated theoretical capillary limit of 4.87 W and experimental peak performance of 4.50 W at the thermal resistance of 1.06 K/W of their ultra-thin heat pipe.

3.4. Evaporator

Evaporator design should focus on the integration of a high thermal conductivity structure layer. The combination of a rigid, high thermal conductivity material at the evaporator and condenser section with a flexible articulating adiabatic section is a potential direction. A strong thermal connection between the shell material and porous wick structure in the evaporator is essential to minimise thermal resistance. A composite polymer and copper design have been shown using thermal vias to reduce through-wall thermal conductivity [79,111]. For a sufficiently thin low thermal conductivity casing material, the temperature drop through the casing may be insignificant compared to the temperature drop across the entire system.

Some literature has noted that in the confined geometry of the flat plate heat pipe, no nucleated boiling occurs despite superheat of 8 K due to large latent heat and surface tension [5,75,76]. Dai et al. [106,126] demonstrated capillary evaporation, utilizing microchannels under a bonded mesh layer. It is essential to implement a composite (bi-porous) evaporator design to prevent a vapour blanket thermal insulator from forming at the evaporator in the case of boiling occurring [63].

Zu et al. [124] investigated flow boiling in ultra-thin flat heat pipes. Their heat pipe consisted of a single-layer wire mesh core structure (~200 count), water as the working fluid, and a 124 mm × 14 mm × 1 mm cavity. During the optimum performance in the nuclear boiling regime, they observed that film boiling is subdued due to the mesh structure and reflow of the condensed work fluid, aiding in bubble detachment. They noted that the bubble size is limited to that of a single mesh pore and the periodic movement of flat bubbles in the vapour space.

3.5. Condenser

Mobile devices are limited by natural convection from the outside shell. To mitigate hot spots on these devices, effective thermal spreading must be achieved. This is tied to the liquid-vapour space ratio.

1. To improve the condenser uniformity, some research has suggested (i) increasing the thermal conduction resistance in the central region of the condenser-side wall and wick, and (ii) reducing the vapour core thermal resistance. One way to achieve both effects is to eliminate parts of the central condenser region's wicking layer. This would locally reduce the wick's effective thermal conductivity in this region by replacing the porous sintered copper with a layer of lower-

conductivity liquid (water). The effective permeability (of the sintered copper wick and the grooves) would increase, allowing for a thinner wick over the entire condenser side inner wall while maintaining the same pressure drop, hence reducing the vapour-core thermal resistance [5].

2. Other research suggests that the combination of a superhydrophobic condenser and superhydrophilic evaporator can significantly improve the vapour chamber's performance. This superhydrophobic surface has several advantages: (i) It can effectively prevent the generation of a liquid film that may significantly degrade the condensation efficiency; (ii) the vapour can easily condense to a droplet on this surface, which then drops down directly into the wick. This can shorten the water feeding route and prevent dry-out in the centre wick [105].

Dropwise condensation has been shown to be significantly more efficient than its filmwise counterpart [127]. Limited studies have been reported on condensation in small confined spaces [128]. Convective dropwise condensation in a small confined cavity, such as an ultra-thin heat pipe, introduces challenges due to wall effects [129]. A way to understand when the condensation process is mainly a capillary phenomenon is to use the drop confinement number (Co):

$$Co = \frac{L_{cap}}{L_{char}} \tag{12}$$

where L_{cap} is the capillary length ($L_{cap} = \sqrt{\sigma/(g\Delta\rho)}$), for a water-vapour system, this is ~2.5 mm [128]. A more appropriate acceleration term for convective condensation in place of g may be the acceleration of the working fluid in the channel, but this is difficult to know at the design stage. L_{char} is the characteristic length, in the case of the an ultra-thin heat pipe this would be the minimum distance between walls inside the internal cavity. When $Co > 1$ droplet departure is confined limiting advantageous departure modes such as jumping, rolling and sliding [130].

3.6. Working fluid

Liu et al. [97] noted that a suitable approximation of the optimum filling ratio was when the working medium is enough to immerse the structure of the capillary mesh.

The choice of a working fluid is crucial in the design of such vapour chambers. Given the principle of operation of a vapour chamber (a two-phase thermodynamic cycle), the fluid's thermophysical properties significantly impact its performance. Patankar et al. [68] defined a separate figure of merit for the vapour (M_v) and liquid (M_l) phases to define the best working fluid for a given geometry.

$$M_l = \frac{\sigma\rho_l h_{fg}}{\mu_l} \tag{13}$$

A higher value for this figure of merit indicates that the vapour chamber can operate at a larger power prior to reaching the capillary limit.

$$M_v = \frac{P_v\rho_v h_{fg}^2}{\mu_v R_g T_v^2} \tag{14}$$

where P_v is the vapour pressure and T_v is the vapour temperature. A higher value for this figure of merit corresponds to a lower thermal resistance in the vapour core. To achieve maximum thermal transfer at minimal thicknesses, a working fluid with a higher M_l is required to minimize the required wick thickness, thus maximizing the available vapour space. Design for ultra-thin heat pipes should maximize both measures to optimize performance. The unique temperature-dependence of thermophysical properties for each fluid governs fluid selection; caution must be exercised to ensure a reasonable vapour pressure at which the vapour chamber's structural integrity is not compromised.

3.7. Modelling limits and transient operation

Analytical and numerical models typically do not capture other phenomena that may result in operational limits to the maximum heat transfer capacity of a heat pipe, such as the entrainment of liquid into the vapour phase by shearing of the interface, local dry out at the evaporator due to boiling, and choking of the vapour flow at the sonic limit [2]. The transient and start-up performance of the heat pipe should also be considered.

4. Conclusions

Ultra-thin flexible heat pipe technology is a rapidly growing field due to the advent of foldable and wearable electronic devices. The realisation of this technology is a complex challenge incorporating evaporation, condensation, two-phase flow, flexible porous wicking structure and flexible impermeable shell material design, all for an ultra-thin package size.

Ultra-thin flexible heat pipes share common design components with macro rigid, ultra-thin rigid, and macro flexible heat pipes. These works provide an excellent foundation for the future development of ultra-thin flexible heat pipes for the cooling of foldable electronics.

From the literature, prominent challenges to overcome include (i) the development of a shell material with suitable flexibility, thermal conductivity, impermeability and the capacity to thermally bond to the implemented porous wicking structure. (ii) multiscale flexible porous wicking structure to enable high capillary pressure, permeability and flexion and (iii) optimisation of the fluid-vapour space design to allow efficient two-phase flow within the flexible heat pipe. These three components are all intrinsically linked, providing an exciting opportunity for future research.

A clear need for research on ultra-thin flexible heat pipes for foldable mobile electronic devices is demonstrated from the discussed material in this study. The proposed research is interdisciplinary in nature, incorporating experimental heat transfer, fluid visualization, analytical and numerical modelling, and material sciences.

Declaration of Competing Interest

The authors declare that they have no known competing financial interests or personal relationships that could have appeared to influence the work reported in this paper.

Acknowledgements

The authors would like to acknowledge the financial support of the Irish Research Council under Grant No. IRC/GOIPD/2019/666.

References

[1] H. Tang, Y. Tang, Z. Wan, J. Li, W. Yuan, L. Lu, Y. Li, K. Tang, Review of applications and developments of ultra-thin micro heat pipes for electronic cooling, Appl. Energy 223 (2018) 383–400, https://doi.org/10.1016/j.apenergy.2018.04.072.

[2] Y. Yadavalli, J.A. Weibel, S.V. Garimella, Performance-governing transport mechanisms for heat pipes at ultrathin form factors, IEEE Trans. Compon. Packag. Manuf. Technol. 5 (2015) 1618–1627, https://doi.org/10.1109/TCPMT.2015.2477275.

[3] J. Lim, S.J. Kim, Fabrication and experimental evaluation of a polymer-based flexible pulsating heat pipe, Energy Convers. Manag. 156 (2018) 358–364, https://doi.org/10.1016/j.enconman.2017.11.022.

[4] H.E. Lall, P. Pecht, MG Influence of temperature on microelectronics and system reliability, CRC Press, 1997.

[5] G. Patankar, J.A. Weibel, S.V. Garimella, Patterning the condenser-side wick in ultra-thin vapor chamber heat spreaders to improve skin temperature uniformity of mobile devices, Int. J. Heat Mass Transf. 101 (2016) 927–936, https://doi.org/10.1016/j.ijheatmasstransfer.2016.05.093.

[6] T.L. Bergman, F.P. Incropera, A.S. Lavine, Fundamentals of heat and mass transfer, Wiley, 2011.
[7] R.B. Wright, J.P. Christophersen, C.G. Motloch, J.R. Belt, C.D. Ho, V.S. Battaglia, J.A. Barnes, T.Q. Duong, R.A. Sutula, Power fade and capacity fade resulting from cycle-life testing of advanced technology development program lithium-ion batteries, J. Power Sources 119–121 (2003) 865–869, https://doi.org/10.1016/S0378-7753(03)00190-3.
[8] V. Chiriac, S. Molloy, J. Anderson, K. Goodson, V. Chiriac, A figure of merit for smart phone thermal management, in: 15th IEEE Intersoc. Conf. Therm. Thermomechanical Phenom. Electron. Syst., IEEE, 2016: pp. 1393–1397. https://doi.org/10.1109/ITHERM.2016.7517712.
[9] F.R. Rothkopf, A.J.M. Janis, T. Dabov, Flexible display devices, US20190053388A1, 2019.
[10] J. Ai, H. Mitchell A., S. Kim, S.R. McClure, Electronic devices with flexible displays and hinges, US20200166974A1, 2020.
[11] D.W. Browning, M. Aleksander, J.L. Zuniga, R.K. Sarraju, G.M. Therien, S. Kamppari, A.C. Younkin, Electronic device with foldable display panels, US OOD789925S, 2017.
[12] J. Yeom, Flexible smart mobile phone, US 00D828321S, 2018.
[13] H. Lee, W. Joo, H. Chae, Portable electronic device, US 009625947B2 (12), 2017.
[14] Y. Fukuma, M. Kinoshita, M. Nakamura, Display, electronic unit, and supporting substrate, US 009013884B2, 2015.
[15] I. Kauhaniem, E. Määttä, L. Hyvönen, J. Ropo, V.C. Alonso, C. Gheorghiu, Bendable device with display in movable connection with body, US 010209801B2, 2019.
[16] I. Kauhaniemi, M. Espoo, L. Hyvönen, J. Ropo, V.C. Alonso, C. Gheorghiu, Bendable device with display in movable connection with body, US 009778772B2, 2017.
[17] R.W.. Harmon, A.R.. Cavallaro, J.P.. Wojack, Three part foldable housing supporting multiple use positions in an electronic device, US 20180077806A1, 2018.
[18] E.-S. Maatta, I. Kauhaniemi, Foldable device, US 009442530B2, 2016.
[19] I. Kauhaniemi, H. Hakamaki, M. Kontkanen, K. Salo, V. Nevalainen, Apparatus and method of providing an apparatus comprising a bendable portion, US 009710021B2, 2017.
[20] C. Kim, Mobile device with touch screens and method of controlling the same, US 20170357473A1, 2017.
[21] J.-H. Park, H.-S. Seo, T. Takayanagi, W. Kaihotsu, Y.-D. Bae, S.-Y. Cho, dae-myung Kim, jae-young Huh, Foldable device, US 20200166972A1, 2020.
[22] S. Yamazaki, Y. Hirakata, H. Ikeda, Display device, US 009780160B2, 2017.
[23] S. Yamazaki, Y. Takemura, Electronic device, US 010228729B2, 2019.
[24] A. Endo, S. Onoya, M. Hiroki, Electronic device, US 010338716B2, 2019.
[25] Y. Hirakata, Display device and manufacturing method thereof, US 010613362B2, 2020.
[26] S. Yamazaki, Y. Yanagisawa, D. Nakamura, N. Sugisawa, H. Ikeda, N. Senda, K. Yoshizumi, Display systemand display device, US 2016O132281A1, 2016.
[27] S. Yamazaki, Display device, electronic device, and system, US 20170038641A1, 2017.
[28] M. Hiroki, A. Endo, Light - emitting device and electronic device, US 20190148656A1, 2019.
[29] Y. Hirakata, A. Endo, Light - emitting device, US 20200109838A1, 2020.
[30] C. Shin, B. Lee, S. Kim, D. Yu, S. Lee, Portable electronic device, US 009829924B2, 2017.
[31] K. Hatano, Light-emitting device, flexible light-emitting device, electronic device, lightingapparatus, and method of manufacturing light-emitting device and flexble-light emitting device, US 009000443B2 (12), 2015.
[32] T. Aoyama, Y. Jinbo, Y. Hirakata, S. Yamazaki, Joining structure of light emitting units, US 010514137B2, 2019.
[33] Y. Yanagisawa, T. Kawata, Display device and electronic device, US 20190348481A1, 2019.
[34] S. Vasylyev, Retractable and curved - shape electronic displays, US 20190383474A1, 2019.
[35] C.D. Jones, D.N. Memering, C.C. Bartlow, Foldable cover and display for an electronic device, US 20200150726A1, 2020.
[36] T. Chang, P.W. Chu, P.J. Cimo, A.J. Ellison, G. Hu, T.M. Gross, N.J. Smith, B.R. Vaddi, N. Venkataraman, Bendable glass stack assemblies , articles and methods of making the same, US 20190050027A1, 2019.
[37] T.-W. Kim, G.-S. Chae, J.-H. Park, N.-J. Myung, S.-H. Lee, T.-H. Kwak, S.-H. Shin, Foldable display device, US 009983424B2, 2018.
[38] N.J. Myung, S.J. Jang, H. Kwak, Foldable plate and foldable display device with the same, US 2016O187931A1, 2016.
[39] Z. Zhang, V.H.. Yin, C.Y.. Liu, P.S.. Drzaic, S. Bae, C.-H. Tung, K. Vakhshouri, S. Kang, J.Z.. Zhong, Electronic devices with flexible displays, US 20170336831 A1, 2017.
[40] J.A. Rogers, K.D. Hyeong, Flexible and stretchable electronic systems for epidermal electronics, US 20200315488A1, 2020. https://patentimages.storage.googleapis.com/44/de/fd/e6cb3f931e9c8f/US20170317558A1.pdf.
[41] J.A. Rogers, H. Yonggang, K.H. Cho, S. Mark, C.W. Mook, S. Jizhou, A.J. Hyun, K. D. Hyeong, Stretchable and foldable electronic devices, US010292261B2, 2019. https://doi.org/10.1177/002205740706502225.
[42] J. Fan, H. Park, Y. Wu, Temperature-regulating garment, US 20170172227A1, 2017.
[43] H.E.A. Huitema, P. Inagaki, Device with flexible electronic components on multiple surfaces, US 10289163B2, 2019.
[44] H.E.A. Huitema, K.W. Mok, S.M. Curry, Support structures for a flexible electronic component, US 009980402 B2, 2018.
[45] C.-W. Chen, C.-W. Kuo, T.-Y. Chang, H.-C. Chuang, Flexible vapor chamber, US 20200326134A1, 2020.
[46] R. Yang, Y.-C. Lee, V.M. Bright, C. Li, C. Oshman, B. Shi, J.-H. Cheng, G.P. Peterson, Thermal ground plane, US 20200191495A1, 2020.
[47] M. Nikkhoo, D. Heirich, R. Riccomini, M. Ye, M. Beerman, J. Daniel, Flexible thermal conduit for an electronic device, US 009986667B2, 2018.
[48] E. Hurbi, M. Nikkhoo, Thermal dissipation system for wearable electronic devices, US 010433467B2, 2019.
[49] C. Van Ho, B.D. Redmond, B.E. Gray, G.R. McClary, Device configuration - based thermal management control, US20190286200A1, 2019.
[50] A.D. Delano, E.E. Hurbi, L.M. Ghioni, Conducting heat through a hinge, US 20190354148A1, 2019.
[51] A.D. Delano, E.E. Hurbi, L.M. Ghioni, Conducting heat through a hinge via flexible vapor chamber, WO 2019221942A1, 2019.
[52] E. Hong, Foldable electronic device, US20200204666A1, 2020.
[53] Y. Xu, Y. Tu, Thermal pad, method for fabricating thermal pad, heat disspatingapparatus and electronic device, US 20140116661A1, 2014.
[54] C. Gheorghiu, E.-S. Määttä, I. Kauhaniemi, Apparatus and method of providing an apparatus comprising a bendable portion, US 009927841B2, 2018.
[55] T.C.. North, C.D.. Hood III, L.E.. Knepper, D.M.. Aurongzeb, J.A.. Abullarade, System and method for dynamic thermal management in passively cooled device with a plurality of display surfaces, US 009964993 B2, 2018.
[56] R.J.. Lewis, R. Yang, Y.-C. Lee, Thermal management planes, US 20180320984A1, 2018.
[57] D.M. JOHNSON, C.L. COBB, Flexible thermal regulation device, US 2016O178251A1, 2016.
[58] Y.J. Kim, H.M. Gu, C.S. Kim, H. Choi, G. Lee, S. Kim, K.K. Yi, S.G. Lee, B.J. Cho, High-performance self-powered wireless sensor node driven by a flexible thermoelectric generator, Energy 162 (2018) 526–533, https://doi.org/10.1016/j.energy.2018.08.064.
[59] Investigation of polymer based micro heat pipes for... - Google Scholar, (n.d.). https://scholar.google.com/scholar?hl=en&as_sdt=0%2C5&q=Investigation+of+polymer+based+micro+heat+pipes+for+a+flexible+spacecraft+radiator&btnG= (accessed April 22, 2021).
[60] H. Hwangbo, T.E. Joost, A flexible variable conductance heat pipe design for temperature control of spacecraft equipment, in: AIAA 23rd Thermophys. Plasmadynamics Lasers Conf. 1988, American Institute of Aeronautics and Astronautics Inc, AIAA, 1998. https://doi.org/10.2514/6.1988-2680.
[61] N.J. Gernert, J. Brown, Development of a flexible loop heat pipe cold plate, in: SAE Tech. Pap., SAE International, 1995. https://doi.org/10.4271/951436.
[62] X. Chen, H. Ye, X. Fan, T. Ren, G. Zhang, A review of small heat pipes for electronics, Appl. Therm. Eng. 96 (2016) 1–17, https://doi.org/10.1016/j.applthermaleng.2015.11.048.
[63] C.W. Chan, E. Siqueiros, J. Ling-Chin, M. Royapoor, A.P. Roskilly, Heat utilisation technologies: A critical review of heat pipes, Renew. Sustain. Energy Rev. 50 (2015) 615–627, https://doi.org/10.1016/j.rser.2015.05.028.
[64] C. Yang, C. Song, W. Shang, P. Tao, T. Deng, Flexible heat pipes with integrated bioinspired design, Prog. Nat. Sci. Mater. Int. 25 (2015) 51–57, https://doi.org/10.1016/j.pnsc.2015.01.011.
[65] L.L. Vasiliev, Heat pipes in modern heat exchangers, Appl. Therm. Eng. (2005), https://doi.org/10.1016/j.applthermaleng.2003.12.004.
[66] A. Faghri, Review and advances in heat pipe science and technology, J. Heat Transf. (2012), https://doi.org/10.1115/1.4007407.
[67] Y. Li, W. Zhou, J. He, Y. Yan, B. Li, Z. Zeng, Thermal performance of ultra-thin flattened heat pipes with composite wick structure, Appl. Therm. Eng. 102 (2016) 487–499, https://doi.org/10.1016/j.applthermaleng.2016.03.097.
[68] G. Patankar, J.A. Weibel, S.V. Garimella, Working-fluid selection for minimized thermal resistance in ultra-thin vapor chambers, Int. J. Heat Mass Transf. 106 (2017) 648–654, https://doi.org/10.1016/j.ijheatmasstransfer.2016.09.038.
[69] G. Patankar, J.A. Weibel, S.V. Garimella, On the transient thermal response of thin vapor chamber heat spreaders: Governing mechanisms and performance relative to metal spreaders, Int. J. Heat Mass Transf. 136 (2019) 995–1005, https://doi.org/10.1016/j.ijheatmasstransfer.2019.03.058.
[70] G. Huang, W. Liu, Y. Luo, T. Deng, Y. Li, H. Chen, Research and optimization design of limited internal cavity of ultra-thin vapor chamber, Int. J. Heat Mass Transf. 148 (2020), 119101, https://doi.org/10.1016/j.ijheatmasstransfer.2019.119101.
[71] K.S. Yang, C.W. Tu, W.H. Zhang, C.T. Yeh, C.C. Wang, A novel oxidized composite braided wires wick structure applicable for ultra-thin flattened heat pipes, Int. Commun. Heat Mass Transf. 88 (2017) 84–90, https://doi.org/10.1016/j.icheatmasstransfer.2017.08.014.
[72] W. Zhou, Y. Li, Z. Chen, L. Deng, Y. Gan, A novel ultra-thin flattened heat pipe with biporous spiral woven mesh wick for cooling electronic devices, Energy Convers. Manag. 180 (2019) 769–783, https://doi.org/10.1016/j.enconman.2018.11.031.
[73] G. Chen, Y. Tang, Z. Wan, G. Zhong, H. Tang, J. Zeng, Heat transfer characteristic of an ultra-thin flat plate heat pipe with surface-functional wicks for cooling electronics, Int. Commun. Heat Mass Transf. 100 (2019) 12–19, https://doi.org/10.1016/j.icheatmasstransfer.2018.10.011.
[74] J. Li, L. Lv, Experimental studies on a novel thin flat heat pipe heat spreader, Appl. Therm. Eng. 93 (2016) 139–146, https://doi.org/10.1016/j.applthermaleng.2015.09.038.
[75] W. Zhou, P. Xie, Y. Li, Y. Yan, B. Li, Thermal performance of ultra-thin flattened heat pipes, Appl. Therm. Eng. 117 (2017) 773–781, https://doi.org/10.1016/j.applthermaleng.2017.01.089.

[76] S.W. Chang, K.F. Chiang, T.H. Lee, Thermal performance of thin loop-type vapor chamber, Exp. Therm Fluid Sci. 61 (2015) 130–143, https://doi.org/10.1016/j.expthermflusci.2014.10.016.

[77] L. Lv, J. Li, Managing high heat flux up to 500 W/cm2 through an ultra-thin flat heat pipe with superhydrophilic wick, Appl. Therm. Eng. 122 (2017) 593–600, https://doi.org/10.1016/j.applthermaleng.2017.05.050.

[78] R. Lewis, L.A. Liew, S. Xu, Y.C. Lee, R. Yang, Microfabricated ultra-thin all-polymer thermal ground planes, Sci. Bull. 60 (2015) 701–706, https://doi.org/10.1007/s11434-015-0760-9.

[79] C. Oshman, B. Shi, C. Li, R. Yang, Y.C. Lee, G.P. Peterson, V.M. Bright, The development of polymer-based flat heat pipes, J. Microelectromech. Syst. 20 (2011) 410–417, https://doi.org/10.1109/JMEMS.2011.2107885.

[80] S. Zhang, J. Chen, Y. Sun, J. Li, J. Zeng, W. Yuan, Y. Tang, Experimental study on the thermal performance of a novel ultra-thin aluminum flat heat pipe, Renew. Energy. 135 (2019) 1133–1143, https://doi.org/10.1016/j.renene.2018.12.097.

[81] C. Yang, C. Chang, C. Song, W. Shang, J. Wu, P. Tao, T. Deng, Fabrication and performance evaluation of flexible heat pipes for potential thermal control of foldable electronics, Appl. Therm. Eng. 95 (2016) 445–453, https://doi.org/10.1016/j.applthermaleng.2015.11.078.

[82] T. Jaipurkar, P. Kant, S. Khandekar, B. Bhattacharya, S. Paralikar, Thermo-mechanical design and characterization of flexible heat pipes, Appl. Therm. Eng. 126 (2017) 1199–1208, https://doi.org/10.1016/j.applthermaleng.2017.01.036.

[83] J. Huang, W. Zhou, J. Xiang, C. Liu, Y. Gao, S. Li, W. Ling, Development of novel flexible heat pipe with multistage design inspired by structure of human spine, Appl. Therm. Eng. 175 (2020), 115392, https://doi.org/10.1016/j.applthermaleng.2020.115392.

[84] S.S. Hsieh, Y.R. Yang, Design, fabrication and performance tests for a polymer-based flexible flat heat pipe, Energy Convers. Manag. 70 (2013) 10–19, https://doi.org/10.1016/j.enconman.2013.02.011.

[85] C. Feng, M. Gibbons, M. Marengo, S. Chandra, A Novel Ultra-Large Flat Plate Heat Pipe Manufactured by Thermal Spray, Appl. Therm. Eng. (2020), 115030, https://doi.org/10.1016/J.APPLTHERMALENG.2020.115030.

[86] H. Aoki, N. Shioya, M. Ikeda, Y. Kimura, Development of ultra thin plate-type heat pipe with less than 1 mm thickness, in: Annu. IEEE Semicond. Therm. Meas. Manag. Symp., 2010, pp. 217–223, https://doi.org/10.1109/STHERM.2010.5444289.

[87] W. Zhou, Y. Li, Z. Chen, L. Deng, Y. Gan, Effect of the passage area ratio of liquid to vapor on an ultra-thin flattened heat pipe, Appl. Therm. Eng. 162 (2019), 114215, https://doi.org/10.1016/j.applthermaleng.2019.114215.

[88] J.A. Weibel, S.V. Garimella, Recent Advances in Vapor Chamber Transport Characterization for High-Heat-Flux Applications, Adv. Heat Transf. 45 (2013) 209–301, https://doi.org/10.1016/B978-0-12-407819-2.00004-9.

[89] Dell, XPS 17 (9700) Laptop, (2020). https://www.dell.com/en-ie/shop/laptops/xps-17-laptop/spd/xps-17-9700-laptop (accessed June 17, 2020).

[90] C. Jung, J. Lim, S.J. Kim, Fabrication and evaluation of a high-performance flexible pulsating heat pipe hermetically sealed with metal, Int. J. Heat Mass Transf. 149 (2020), 119180, https://doi.org/10.1016/j.ijheatmasstransfer.2019.119180.

[91] G. Huang, W. Liu, Y. Luo, Y. Li, H. Chen, Fabrication and thermal performance of mesh-type ultra-thin vapor chambers, Appl. Therm. Eng. 162 (2019), 114263, https://doi.org/10.1016/j.applthermaleng.2019.114263.

[92] Z. Chen, Y. Li, W. Zhou, L. Deng, Y. Yan, Design, fabrication and thermal performance of a novel ultra-thin vapour chamber for cooling electronic devices, Energy Convers. Manag. 187 (2019) 221–231, https://doi.org/10.1016/j.enconman.2019.03.038.

[93] C. Ding, G. Soni, P. Bozorgi, B.D. Piorek, C.D. Meinhart, N.C. MacDonald, A flat heat pipe architecture based on nanostructured titania, J. Microelectromech. Syst. 19 (2010) 878–884, https://doi.org/10.1109/JMEMS.2010.2051019.

[94] G.-W. Wu, S.-L. Chen, W.-P. Shih, Lamination and Characterization of a Polyethylene-Terephthalate Flexible Micro Heat Pipe, in: 10th Int. Heat Pipe Symp., 2011: pp. 80–85. https://doi.org/10.5098/fhp.v3.2.3003.

[95] C. Oshman, Q. Li, L.A. Liew, R. Yang, V.M. Bright, Y.C. Lee, Flat flexible polymer heat pipes, J. Micromech. Microeng. 23 (2013), 015001, https://doi.org/10.1088/0960-1317/23/1/015001.

[96] D. Lee, C. Byon, Fabrication and characterization of pure-metal-based submillimeter-thick flexible flat heat pipe with innovative wick structures, Int. J. Heat Mass Transf. 122 (2018) 306–314, https://doi.org/10.1016/j.ijheatmasstransfer.2018.01.135.

[97] C. Liu, Q. Li, D. Fan, Fabrication and performance evaluation of flexible flat heat pipes for the thermal control of deployable structure, Int. J. Heat Mass Transf. 144 (2019), 118661, https://doi.org/10.1016/j.ijheatmasstransfer.2019.118661.

[98] National Research Council, Assessment of advanced solid-state lighting, National Academies Press, 2013.

[99] T. Kawabata, Y. Ohno, Optical measurements of OLED panels for lighting applications, J. Mod. Opt. 60 (2013) 1176–1186, https://doi.org/10.1080/09500340.2013.806681.

[100] H.T. Chen, W.C.H. Choy, S.Y. Hui, Characterization, Modeling, and Analysis of Organic Light-Emitting Diodes With Different Structures, IEEE Trans. Power Electron. 31 (2016) 581–592, https://doi.org/10.1109/TPEL.2015.2403618.

[101] A.B. Solomon, K. Ramachandran, B.C. Pillai, Thermal performance of a heat pipe with nanoparticles coated wick, Appl. Therm. Eng. 36 (2012) 106–112, https://doi.org/10.1016/j.applthermaleng.2011.12.004.

[102] S.C. Wong, S.F. Huang, K.C. Hsieh, Performance tests on a novel vapor chamber, Appl. Therm. Eng. 31 (2011) 1757–1762, https://doi.org/10.1016/j.applthermaleng.2011.02.020.

[103] J.C. Hsieh, H.J. Huang, S.C. Shen, Experimental study of microrectangular groove structure covered with multi mesh layers on performance of flat plate heat pipe for LED lighting module, Microelectron. Reliab. 52 (2012) 1071–1079, https://doi.org/10.1016/j.microrel.2011.11.016.

[104] C. Wang, Z. Liu, G. Zhang, M. Zhang, Experimental investigations of flat plate heat pipes with interlaced narrow grooves or channels as capillary structure, Exp. Therm. Fluid Sci. 48 (2013) 222–229, https://doi.org/10.1016/j.expthermflusci.2013.03.004.

[105] Z. Sun, H. Qiu, An asymmetrical vapor chamber with multiscale micro/nanostructured surfaces, Int. Commun. Heat Mass Transf. 58 (2014) 40–44, https://doi.org/10.1016/j.icheatmasstransfer.2014.08.027.

[106] X. Dai, F. Yang, R. Yang, Y.C. Lee, C. Li, Micromembrane-enhanced capillary evaporation, Int. J. Heat Mass Transf. 64 (2013) 1101–1108, https://doi.org/10.1016/j.ijheatmasstransfer.2013.05.030.

[107] Y. Peng, W. Liu, B. Liu, J. Liu, K. Huang, L. Wang, W. Chen, The performance of the novel vapor chamber based on the leaf vein system, Int. J. Heat Mass Transf. 86 (2015) 656–666, https://doi.org/10.1016/j.ijheatmasstransfer.2015.01.126.

[108] M.R. Shaeri, D. Attinger, R. Bonner, Feasibility study of a vapor chamber with a hydrophobic evaporator substrate in high heat flux applications, Int. Commun. Heat Mass Transf. 86 (2017) 199–205, https://doi.org/10.1016/j.icheatmasstransfer.2017.05.028.

[109] D. Deng, Q. Huang, Y. Xie, X. Huang, X. Chu, Thermal performance of composite porous vapor chambers with uniform radial grooves, Appl. Therm. Eng. 125 (2017) 1334–1344, https://doi.org/10.1016/j.applthermaleng.2017.07.108.

[110] M. Ivanova, A. Lai, C. Gillot, N. Sillon, C. Schaeffer, F. Lefèvre, M. Lallemand, E. Fournier, Design, fabrication and test of silicon heat pipes with radial microcapillary grooves, Thermomech. Phenom. Electron. Syst. (2006) 545–551, https://doi.org/10.1109/ITHERM.2006.1645392.

[111] K.S. Yang, T.Y. Yang, C.W. Tu, C.T. Yeh, M.T. Lee, A novel flat polymer heat pipe with thermal via for cooling electronic devices, Energy Convers. Manag. 100 (2015) 37–44, https://doi.org/10.1016/j.enconman.2015.04.063.

[112] J. Li, L. Lv, G. Zhou, X. Li, Mechanism of a microscale flat plate heat pipe with extremely high nominal thermal conductivity for cooling high-end smartphone chips, Energy Convers. Manag. 201 (2019), 112202, https://doi.org/10.1016/j.enconman.2019.112202.

[113] A. Nematollahisarvestani, R.J. Lewis, Y.C. Lee, Design of Thermal Ground Planes for Cooling of Foldable Smartphones, J. Electron. Packag. Trans. ASME. 141 (2019), 021004, https://doi.org/10.1115/1.4042472.

[114] C. Oshman, Q. Li, L.A. Liew, R. Yang, Y.C. Lee, V.M. Bright, D.J. Sharar, N. R. Jankowski, B.C. Morgan, Thermal performance of a flat polymer heat pipe heat spreader under high acceleration, J. Micromech. Microeng. 22 (2012), https://doi.org/10.1088/0960-1317/22/4/045018.

[115] B.D. Marcus, Theory and design of variable conductance heat pipes, (1972).

[116] A. Faghri, Heat pipe science and technology, Global Digital Press, 1995.

[117] J.A. Weibel, S.V. Garimella, Visualization of vapor formation regimes during capillary-fed boiling in sintered-powder heat pipe wicks, Int. J. Heat Mass Transf. 55 (2012) 3498–3510, https://doi.org/10.1016/j.ijheatmasstransfer.2012.03.021.

[118] C. Feng, S. Yugeswaran, S. Chandra, Capillary rise of liquids in thermally sprayed porous copper wicks, Exp. Therm. Fluid Sci. 98 (2018) 206–216, https://doi.org/10.1016/j.expthermflusci.2018.05.031.

[119] J. Liu, Y. Zhang, C. Feng, L. Liu, T. Luan, Study of copper chemical-plating modified polyacrylonitrile-based carbon fiber wick applied to compact loop heat pipe, Exp. Therm Fluid Sci. 100 (2019) 104–113, https://doi.org/10.1016/j.expthermflusci.2018.07.008.

[120] L. Zhao, F. Qiang, S.W. Dai, S.C. Shen, Y.Z. Huang, N.J. Huang, G.D. Zhang, L. Z. Guan, J.F. Gao, Y.H. Song, L.C. Tang, Construction of sandwich-like porous structure of graphene-coated foam composites for ultrasensitive and flexible pressure sensors, Nanoscale 11 (2019) 10229–10238, https://doi.org/10.1039/c9nr02672j.

[121] W. Song, J. Zhu, B. Gan, S. Zhao, H. Wang, C. Li, J. Wang, Flexible, Stretchable, and Transparent Planar Microsupercapacitors Based on 3D Porous Laser-Induced Graphene, Small 14 (2018) 1702249, https://doi.org/10.1002/smll.201702249.

[122] L. Cheng, G. Xia, Fundamental issues, mechanisms and models of flow boiling heat transfer in microscale channels, Int. J. Heat Mass Transf. 108 (2017) 97–127, https://doi.org/10.1016/j.ijheatmasstransfer.2016.12.003.

[123] J. Zhong, J. Riordon, S.H. Zandavi, Y. Xu, A.H. Persad, F. Mostowfi, D. Sinton, Capillary Condensation in 8 nm Deep Channels, J. Phys. Chem. Lett. 9 (2018) 497–503, https://doi.org/10.1021/acs.jpclett.7b03003.

[124] S. Zu, X. Liao, Z. Huang, D. Li, Q. Jian, Visualization study on boiling heat transfer of ultra-thin flat heat pipe with single layer wire mesh wick, Int. J. Heat Mass Transf. 173 (2021), 121239, https://doi.org/10.1016/j.ijheatmasstransfer.2021.121239.

[125] Y.P. Hu, Y.R. Li, C.M. Wu, S.Z. Li, M.H. Li, Flow pattern and heat transfer in Rayleigh-Bénard convection of cold water near its density maximum in a rectangular cavity, Int. J. Heat Mass Transf. 107 (2017) 1065–1075, https://doi.org/10.1016/j.ijheatmasstransfer.2016.11.013.

[126] X. Dai, M. Famouri, A.I. Abdulagatov, R. Yang, Y.C. Lee, S.M. George, C. Li, Capillary evaporation on micromembrane-enhanced microchannel wicks with atomic layer deposited silica, Appl. Phys. Lett. 103 (2013) 18–23, https://doi.org/10.1063/1.4824439.

[127] H. Cha, H. Vahabi, A. Wu, S. Chavan, M.K. Kim, S. Sett, S.A. Bosch, W. Wang, A. K. Kota, N. Miljkovic, Dropwise condensation on solid hydrophilic surfaces, Sci. Adv. 6 (2020), https://doi.org/10.1126/sciadv.aax0746.

[128] J. Yuan, Y. Wang, J. Xu, X. Ji, J. Xie, Convective dropwise condensation heat transfer in mini-channels with biphilic surface, Int. J. Heat Mass Transf. 134 (2019) 69–84, https://doi.org/10.1016/j.ijheatmasstransfer.2019.01.015.
[129] J. Xu, X. Yu, W. Jin, Porous-wall microchannels generate high frequency "eye-blinking" interface oscillation, yielding ultra-stable wall temperatures, Int. J. Heat Mass Transf. 101 (2016) 341–353, https://doi.org/10.1016/j.ijheatmasstransfer.2016.05.039.
[130] J. Xie, J. Xu, W. Shang, K. Zhang, Dropwise condensation on superhydrophobic nanostructure surface, part II: Mathematical model, Int. J. Heat Mass Transf. 127 (2018) 1170–1187, https://doi.org/10.1016/j.ijheatmasstransfer.2018.07.008.